Atmospheric
Chemistry
and Physics
Discussions

Open Access

EGU

1 **Seasonal patterns of atmospheric mercury in tropical South America as inferred by a**

2 **TGM continuous record at the Chacaltaya Station (5240 m) in Bolivia**

3

4 **Authors:**

5 Alkuin Maximilian Koenig[1], Olivier Magand[1], Paolo Laj[1], Marcos Andrade[2,7], Isabel Moreno[2], Fernando

6 Velarde[2], Grover Salvatierra[2], René Gutierrez[2], Luis Blacutt[2], Diego Aliaga[3], Thomas Reichler[4], Karine

7 Sellegri[5], Olivier Laurent[6], Michel Ramonet[6], and Aurélien Dommergue[1]

8

9 **Affiliations**

10 [1] Institut des Géosciences de l'Environnement, Université Grenoble Alpes, CNRS, IRD, Grenoble INP, Grenoble,

11 France

12 [2] Laboratorio de Física de la Atmósfera, Instituto de Investigaciones Físicas, Universidad Mayor de San Andrés,

13 La Paz, Bolivia

14 [3] Institute for Atmospheric and Earth System Research/Physics, Faculty of Science, University of Helsinki,

15 Helsinki, 00014, Finland

16 [4] Department of Atmospheric Sciences, University of Utah, Salt Lake City, 84112, USA

17 [5] Université Clermont Auvergne, CNRS, Laboratoire de Météorologie Physique, UMR 6016, Clermont-Ferrand,

18 France

19 [6] Laboratoire des Sciences du Climat et de l'Environnement, LSCE-IPSL (CEA-CNRS-UVSQ), Université Paris-

20 Saclay, 91191 Gif-sur-Yvette, France

21 [7] Department of Atmospheric and Oceanic Sciences, University of Maryland, College Park, MD, USA

22

23

24 Correspondence to: alkuin-maximilian.koenig@univ-grenoble-alpes.fr

25

26

27 **Abstract**

28 High-quality data of atmospheric mercury (Hg) is rare for South America, especially for its tropical part. In

29 consequence, mercury dynamics are still highly uncertain in this region, a significant deficiency, as South America

30 appears to play a major role in the global budget of this toxic pollutant. To address this issue, we performed nearly

31 two years (July 2014 - February 2016) of continuous high resolution total gaseous mercury (TGM) measurements

32 at the Chacaltaya (CHC) mountain site in the Bolivian Andes, which is subject to a diverse mix of air masses

33 coming predominantly from the Altiplano and the Amazon rainforest. For the first eleven months of

34 measurements, we obtained a mean TGM concentration of $0.89 \pm 0.01\ ng\ m^{-3}$, in good agreement with the

35 sparse amount of data available from the continent. For the remaining nine months, we obtained a significantly

36 higher TGM concentration of $1.34 \pm 0.01\ ng\ m^{-3}$, a difference which we tentatively attribute to the strong "El

37 Niño" event of 2015 - 2016. Based on HYSPLIT back-trajectories and clustering techniques, we show that lower

38 mean TGM concentrations were linked to either westerly Altiplanic air masses or those originating from the

39 lowlands to the south-east of CHC. Elevated TGM concentrations were related to northerly air masses of

40 Amazonian or southerly air masses of Altiplanic origin, the former possibly linked to artisanal and small scale

41 gold mining (ASGM), while the latter might be explained by volcanic activity. We observed a marked seasonal

42 pattern, with low TGM concentrations in the dry season (austral winter), rising concentrations during biomass

43 burning (BB) season, and highest concentrations at the beginning of the wet season (austral summer). With the

44 help of simultaneously sampled equivalent black carbon (eBC) and carbon monoxide (CO) data, we use the clearly

45 BB influenced signal during BB season (August to October) to derive a mean TGM/CO emission ratio of $(2.3 \pm$

46 $0.6) \cdot 10^{-7} ppbv_{TGM}\ ppbv_{CO}^{-1}$, which could be used to constrain South American BB emissions. Through the

47 link with in-situ measured CO_2 and remotely sensed solar-induced fluorescence (SIF) as proxies for vegetation

48 activity, we detect signs of a vegetation sink effect in Amazonian air masses and derive a "best guess" TGM/CO_2

49 *uptake ratio* of $0.058 \pm 0.017\ (ng\ m^{-3})_{TGM}\ ppm_{CO2}^{-1}$. Finally, significantly higher Hg concentrations in

50 western Altiplanic air masses during the wet season as compared to the dry season point towards the modulation

51 of atmospheric Hg by the Eastern Pacific Ocean.

52

1. Introduction

54 Mercury (Hg) is a global contaminant that accumulates in the marine food chain and thus threatens wildlife and

55 populations relying on halieutic resources. In 2017, the Minamata convention was implemented to decrease human

56 exposure to this toxic compound by targeting particularly anthropogenic Hg emissions. It is estimated that

57 humanity has increased atmospheric Hg concentrations by a factor of ~2.6 since the pre-industrial era and that

58 legacy Hg is being recycled in the environment (Beal et al., 2014; Lamborg et al., 2014, Obrist et al., 2018). As

59 reported in the 2018 Global Mercury Assessment, anthropogenic sources of Hg comprise mainly artisanal and

60 small scale gold mining (ASGM, accounting for about 38% of the total emissions in 2015), stationary fossil fuel

61 and biomass combustion (24%), metal and cement production (combined 26%) and garbage incineration (7%).

62 Hg exists in the atmosphere mostly as gaseous elemental mercury (GEM) and oxidized gaseous species (GOM),

63 with the sum of both often being referred to as total gaseous mercury (TGM). Over the last 15 years, TGM and

64 GEM are being monitored worldwide by regional, national, and continental initiatives alongside networks such

65   as GMOS (Global Mercury Observation System), AMNet (Atmospheric Mercury Network), MDN (Mercury

66   Deposition Network), and APMMN (Asia-Pacific Mercury Monitoring Network). These measurements provide

67   a tool to rapidly follow changes and patterns in sources and understand regional processes.

68   Nevertheless, the global coverage of these measurements is far from evenly distributed. While many monitoring

69   sites exist in the Northern Hemisphere, especially China, North America, and Europe, surface observations are

70   sparse in the tropics and the Southern Hemisphere (Howard et al., 2017; Obrist et al., 2018; Sprovieri et al., 2016;

71   Global Mercury Assessment, 2018). In South America, only a few studies have observations to explore the

72   seasonal and multiannual trends of atmospheric Hg. Guédron et al. (2017) give a short record of TGM measured

73   at the Titicaca lake in the Bolivian/Peruvian Andes, while Dieguez et al. (2019) provided a multi-annual, but not

74   continuous record of atmospheric Hg species in Patagonia, Argentina. GEM averages for Manaus in the Amazon

75   rainforest of Brazil were also reported by Sprovieri et al. (2016). Müller et al. (2012) measured TGM during 2007

76   in Nieuw Nickerie, Suriname, in the Northern part of South America, Lastly, some data on tropospheric TGM

77   concentrations is provided by CARIBIC flights (https://www.caribic-atmospheric.com/) for the routes Frankfurt

78   to São Paulo and São Paulo to Santiago de Chile (Slemr et al., 2009, 2016).

79   This lack of data is problematic, as South America plays an important role in the global mercury budget. In 2015,

80   about 18% of global mercury emissions occurred on this continent, where widespread ASGM is thought to be the

81   major contributor (Global Mercury Assessment, 2018). Worldwide, around 53% of the estimated ASGM releases

82   are attributed to South America, but the uncertainties regarding their exact quantity and spatial distribution are

83   large (Global Mercury Assessment, 2018). Furthermore, the role of the world's largest tropical rainforest, the

84   Amazon, has not yet been clearly determined, even though this large pool of vegetation may importantly modulate

85   the seasonal cycle of mercury (Jiskra et al., 2018) through mechanisms such as the substantial storage of Hg in

86   plant litter (Jiskra et al., 2015) and a posteriori re-emission in large-scale biomass burning (BB) events (Fraser et

87   al., 2018; Webster et al., 2016). The highly vegetated Amazon region is very sensitive to external changes (Phillips

88   et al., 2008) and undergoes a constant shift in behavior. On the one hand, there are natural changes, like the El-

89   Niño-Southern Oscillation (ENSO), which strongly affects moisture transport and precipitation over South

90   America and the Amazon (Ambrizzi et al., 2004; Erfanian et al., 2017). On the other hand, there are anthropogenic

91   perturbations, like land-use and climate changes. Both types of variations may greatly and durably alter the

92   equilibrium of the Amazon rainforest ecosystem, with important regional and global consequences (Obrist et al.,

93   2018; Phillips et al., 2008).

94   The goal of this study is to partly overcome the TGM data gap over South America by providing new high-quality

95   Hg measurements from the Global Atmosphere Watch (GAW) station Chacaltaya (CHC), a distinctive site due to

96   its location in the tropical part of the Andes, at 5240 m above sea level. Between July 2014 and February 2016,

97   we continuously measured TGM at the CHC station, which allowed us to sample air masses of both Altiplanic

98   and Amazonian origin. Through this unique data set, we explore the seasonal pattern of TGM in the region and

99   discuss possible sources and sinks for atmospheric mercury in the South American tropics.

100

2. Methodology

2.1 Site description

101
102
103 Measurements were conducted at the CHC GAW regional station (WMO region III – South America, 16°21.0140
104 S, 68°07.8860 W), at an altitude of 5240 m a.s.l, about 140 m below the summit of mount Chacaltaya on the
105 eastern edge of the "Cordillera Real" (Fig. 1, Andrade et al., 2015), with a horizon open to the South and West.
106 Measurements of general meteorology, CO_2, CO, CH_4, O_3 and aerosol properties are performed continuously. The
107 area surrounding the station is stony, sparsely vegetated and with intermittent snow cover (especially in the wet
108 season). The site is located at about 17 km north of the urban agglomeration La Paz/El Alto with more than 1.8
109 million inhabitants and in spite of its high elevation, it is frequently influenced by air masses arriving from the
110 boundary layer of the Altiplano. Thermally-induced circulation is regularly observed between about 9:00 and
111 12:00 local time through an increase in equivalent black carbon (eBC), carbon monoxide (CO), and particulate
112 matter (Andrade et al., 2015; Rose et al., 2017, Wiedensohler et al., 2018). However, cleaner conditions can be
113 observed during nighttime, when the site lies in quasi-free tropospheric conditions (Andrade et al., 2015;
114 Chauvigné et al., 2019; Rose et al., 2017).

115 CHC is relatively close (~300 km distance) to the "Madre de Dios" watershed, a known hot spot for ASGM (Beal
116 et al., 2013; Diringer et al., 2015, 2019). Apart from this prominent region, many other sites of ASGM exist in the
117 Bolivian, Peruvian and Brazilian lowlands, but little exact information is available due to their intrinsically poorly
118 documented and unregulated nature.

119 Finally, starting in northern Chile, extending all along the Bolivia-Chile border and reaching into Peru, we find
120 the central volcanic zone (CVZ), where several volcanoes have been reported to be actively degassing, both to the
121 south (Tamburello et al., 2014; Tassi et al., 2011) and to the west of CHC (Moussallam et al., 2017). This entire
122 volcanic arc showed above long-term average SO_2 emissions in 2015 (Carn et al., 2017).

123
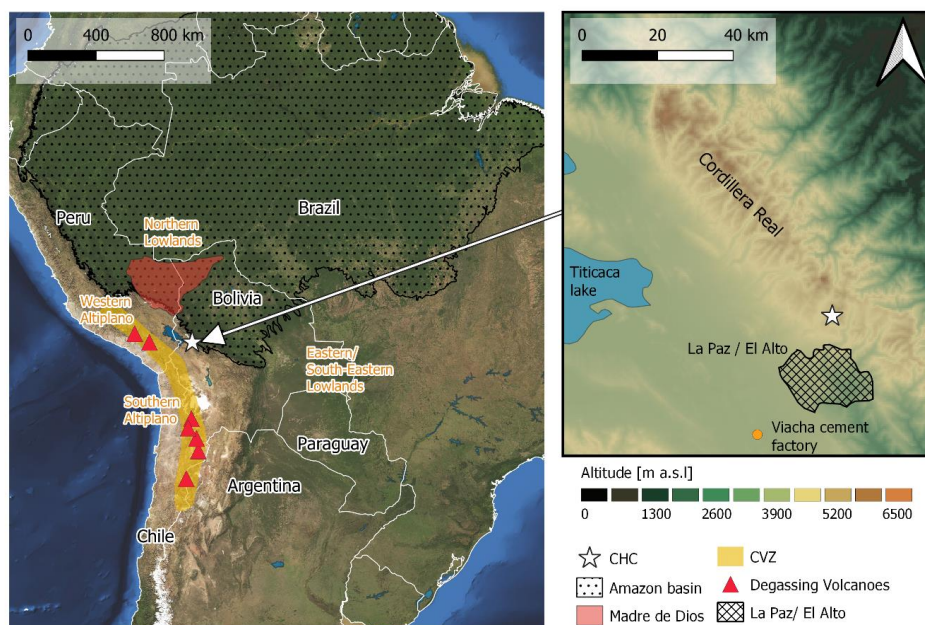
Fig. 1 : *Left: True color satellite image (from ESRI) of the location of CHC station (star) on the continent, with the "Madre de Dios" watershed shaded in red, the Central Volcanic Zone (CVZ) in yellow and the extent of the amazon basin as dotted surface (used Amazon shapefile: http://worldmap.harvard.edu/data/geonode:amapoly_ivb). Air mass origins as used in this work in orange. Selected degassing volcanoes in the CVZ are shown as red triangles, from north to south: Sabancaya, Ubinas, Ollague, San Pedro, Putana, Lascar, Lastarria. Right: Zoomed in map with color coded elevation. The hatched area represents the metropolitan area of La Paz /El Alto, the orange dot shows the cement factory "Cemento Soboce" in the town of Viacha.*

2.2 Data

2.2.1 TGM measurements

Atmospheric total gaseous mercury (TGM) has been measured at CHC GAW station from July 2014 to February 2016, using a 2537A Tekran analyzer model (Tekran Inc., Toronto, Canada). Concentrations are expressed in nanograms per cubic meter at STP conditions (273.15 K, 1013.25 hPa). The instrument is based on mercury enrichment on a gold cartridge, followed by thermal desorption and detection by cold vapour atomic fluorescence spectroscopy (CVAFS) at 253.7 nm (Fitzgerald and Gill, 1979; Bloom and Fitzgerald, 1988). Switching between two cartridges allows for alternating sampling and desorption and thus results in full temporal coverage of the atmospheric mercury measurement. During the 20-month measurement period, the instrument was automatically calibrated every 4 days on average, using an internal mercury permeation source. The latter was annually checked against manual injections of saturated mercury vapor taken from a temperature-controlled vessel, using a Tekran 2505 mercury vapor calibration unit and a Hamilton digital syringe, and following a strict procedure adapted from

145   Dumarey et al (1985). Atmospheric air, sampled through an unheated and UV protected PTFE sampling line and

146   inlet installed outside at 6 m a.g.l., was previously filtered by two 4.5 µm and 0.5 µm 47 mm filters before entering

147   the Tekran, in order to prevent any particulate matter to be introduced into the detection system.

148   The range of TGM concentrations measured during the entire period (43 732 data points) was 0.42 to 4.55 ng m^{-3}

149   , with the detection limit of the instrument being below 0.1 ng m^{-3}. Given a time resolution of 15 min and a

150   sampling flow rate of 0.70 l (STP) min^{-1}, this corresponds to mercury mass loads on the gold cartridges between

151   ~ 5 pg and ~ 48 pg per cycle (average collection of 11.3 pg), and 54% and 81% of the mercury loading per cycle

152   being above 10 and 8 pg, respectively.

153   Since the instrument is limited by local low pressure (540 mbar) at the high altitude CHC station and considering

154   the range of detected concentrations, the default peak integration parameters were quickly optimized to avoid any

155   low bias of measurements due to the internal Tekran integration procedure (Ambrose, 2017; Slemr et al., 2016a;

156   Swartzendruber et al., 2009). Non-linear integration responses for mercury mass loading below 10 pg per cycle

157   have been observed with non-adjusted parameters that control the detection of the end of the peak (NBase and

158   VBase). The latter were improved as stated by Swartzendruber et al. (2009), ensuring high-quality detection

159   conditions in this very atypical atmospheric station, the highest in the world, where the Tekran analyzer, as well

160   as all measurement systems, run in very stringent environmental conditions.

161   To ensure the comparability of the mercury measurements regardless of the study site, the Tekran instrument has

162   been operated according to the GMOS (Global Mercury Observation System) standard operating procedures

163   (SOP, Munthe et al., 2011), in accordance with best practices on measurements adopted in well-established

164   regional mercury monitoring networks (CAMNet, AMNet). Raw dataset, routine, and exceptional

165   maintenance/monitoring files were compiled and processed by software developed at IGE and specifically

166   designed to quality assure and quality control atmospheric mercury datasets in order to produce clean TGM time

167   series. In this automated process, the raw dataset is compared against potential flags corresponding to more than

168   40 criteria that specifically refer to all operation phases related to the calculation of mercury concentrations and

169   calibration (D'Amore et al., 2015). Each raw observation is individually flagged depending on the result of each

170   corresponding criterion and returns, as a temporary output, a flagged dataset (valid, warning, and invalid).

171   Inclusion of all field notes, implying corrections and invalidations of data regrouped in the flagged dataset step,

172   as well as a clarification step by the site manager according to his knowledge allows for the production of a

173   complete QAed/QCed dataset according to the initial temporal acquisition resolution.

174

175   **2.2.2   CO measurements**

176   Atmospheric CO mixing ratio was measured at CHC with a 1-min integration time using a non-dispersion cross-

177   modulation infrared analyzer (model APMA-370, HORIBA Inc.). The sample air was pulled from the outside at

178   about 0.8 L min^{-1} through a 2-m Teflon line. The lower detectable limit is 50 [nmol mol^{-1}] and the instrument was

179   set up to measure in the scale of 0-5 [µmol mol^{-1}].

180

181   **2.2.3   eBC measurements**

182   At CHC, the atmospheric black carbon mass concentration is continuously measured by a Multi-Angle Absorption

183   Photometer (MAAP) (model 5012, Thermo Inc.). The MAAP is a filter-based instrument that utilizes a

184   combination of light reflection and transmission measurements at 637 nm (Müller et al., 2011) together with a

185   radiative transfer model to yield the black carbon concentration using a constant MAC of 6.6 $m^2\,g^{-1}$ (Petzold &

186   Schönlinner, 2004). As black carbon by definition cannot be unambiguously measured with filter-based

187   instruments, it's customary to call the measured light absorbing constituent as equivalent black carbon (eBC)

188   (Bond & Bergstrom, 2006). The sample air is conducted to the instrument through 1.5 meters of a conductive tube

189   from the main inlet that is equipped with an automatic heating system and a whole-air sampling head. Data based

190   on 1-min were recorded, and their hourly averages were used for the analysis given a detection limit of 0.005 µg

191   m^{-3}.

192

2.2.4   CO₂ measurements

194   Atmospheric CO_2 concentrations have been measured with a cavity ring-down spectrometer (CRDS) analyzer

195   from Picarro (model: G2301). This analyzer measures every 2-3 seconds the concentration of CO_2, CH_4 and H_2O.

196   The analyzer was calibrated upon a suite of four calibrated compressed air cylinders provided by LSCE central

197   laboratory (calibrated against the WMO scale) every two to four weeks, and quality control of the data was ensured

198   by regular analysis of two target gases (with known and calibrated concentrations); one short term target gas

199   analyzed for 30 min at least twice a day and one long term target gas analyzed for 30 min during the calibration

200   procedure. Those regular measurements indicate a repeatability of 0.04 ppm. Ambient air is pumped from the roof

201   platform through a dekabon tubing. The Picarro analyzer enables the measurement of atmospheric moisture

202   content, which is used to correct the measured GHG concentrations.

203

2.2.5   Hourly data averaging

205   We generally worked with hourly averages to allow for easy synchronization of measurements from different

206   instruments. Hourly averages were based on the arithmetic mean of all data taken within an hour (starting at 0 and

207   ending at 59 minutes). In the case of TGM, if more than 50% of the singular data points within an hour were

208   invalid (missing data or flagged as bad data), a no-data value was assigned to the respective hourly average and it

209   was excluded from further analysis. In the case of CO_2, were measurements were obtained every few seconds, the

210   hourly averages were based on previously computed minute averages.

211

2.2.6   Uncertainties and confidence intervals

213   All uncertainties of mean concentrations are expressed as two times the standard error of the mean (SEM), giving

214   approximately a 95% confidence interval when comparing subsets of data measured at CHC, under the assumption

215   of constant systematic uncertainty. When comparing CHC data to other stations, we suggest using this value only

216   if it is higher than the average estimated systematic uncertainty for the respective instrument. In the case of the

217   Tekran analyzer, this is about 10% of the measured value (Slemr et al., 2015).

218   The approximately 95% confidence interval for medians in box plots, shown as a notch, is based on the equation

219    $median_{upper/lower} = median \pm 1.58 \cdot \frac{IQR}{\sqrt{n}}$ (McGill et al., 1978). As in the case of the SEM, we advise using

220   the systematic uncertainty of the respective instrument when comparing to other measurement sites.

221 Robust linear models (iteratively reweighted least squares) and their confidence intervals at a level of 95% were
222 computed using the MASS package for R (Venables and Ripley, 2002). Confidence intervals are displayed in
223 square brackets.
224
225   **2.2.7   Solar induced fluorescence (SIF/ SIFTER)**
226 As a remotely sensed proxy for vegetation activity, we examined satellite data on solar induced fluorescence
227 (SIF). More concretely, the SIFTER v2 product described in Koren et al. (2018), provided under the DOI
228 https://doi.org/10.18160/ECK0-1Y4C , and based on the TEMIS SIFTER v2 product, which uses GOME-2A data
229 (Kooreman et al., 2020). SIF has been shown previously to be a good proxy for photosynthetic activity and gross
230 primary production (GPP) (Frankenberg et al., 2011; Koren et al., 2018; Sanders et al., 2016; Zhang et al., 2014).
231 Particularly, satellite obtained SIF is thought to be a more direct measure of plant chemistry than retrieval products
232 based on spectral reflectance, such as the NDVI and EVI (Luus et al., 2017; Zhang et al., 2014). Following the
233 same procedure as described in Koren et al. (2018), we accounted for GOME-2A sensor degradation by linear
234 detrending and obtained an identical time series for the average monthly SIFTER over the entire (legal) Amazon
235 rainforest, which we later used as a proxy for amazon GPP to establish a connection between the variation in
236 mercury levels and vegetation activity (The amazon mask can be found here: doi:10.18160/P1HW-0PJ6).
237
238   **2.2.8   The Oceanic Niño Index (ONI)**
239 To assess the possible influence of "El Nino Southern Oscillation" (ENSO), we deployed the ONI index, which
240 is based on the sea surface temperature (SST) anomaly in the Nino 3-4 region (5N - 5S, 170W - 120W). It is the
241 main index used by NOAA to evaluate the strength of ENSO events and can be obtained at:
242 https://origin.cpc.ncep.noaa.gov/products/analysis_monitoring/ensostuff/ONI_v5.php
243
244   **2.3 Definition of seasonal periods**
245 Air masses arriving at CHC have been reported to show a strong seasonal dependency, both in their origin and
246 the magnitude of biomass burning (BB) influence (Chauvigné et al., 2019; Rose et al., 2015). As in previous
247 studies about CHC station, we grouped the year into three main seasonal periods ("seasons"), which we define as
248 follows:
249   ● The not strongly BB impacted part of the dry season (Here short: Dry season) from May to the end of
250   July, climatologically characterized by predominant highland (Altiplanic) influences and low moisture
251   content. Part of austral winter.
252   ● The BB season from August to the end of October. During this time of the year, forest fires tend to be
253   most common in the region (Graciela et al., 2011; Morgan et al., 2019, also compare to Fig. A1 in
254   Appendix A) and important BB influences are registered at CHC. At the beginning climatologically
255   comparable to the dry season, but with quickly increasing lowland influences along its course.
256   ● The wet season from December to the end of March. During this time of the year, lowland (Amazonian)
257   influences and moisture content are highest and BB is mostly insignificant. This season coincides with
258   austral summer.
259

260 We furthermore considered the remaining months of the year, April and November, to be "transition months"
261 between the mentioned seasons and did not include them in the seasonal analysis.

2.4 Air mass origin at the regional scale

263 To identify common pathways of air mass origin and transport, we used the same set of HYSPLIT back trajectories
264 as already described in Chauvigné et al. (2019). Briefly, for every hour of the day, a 96-hour runtime HYSPLIT
265 back trajectory (Stein et al., 2015) was computed for each of nine arrival points located at 500 meter above ground,
266 and within a 2 km x 2 km square grid around the station. The input meteorological fields for the HYSPLIT
267 simulations were obtained from ERA interim and dynamically downscaled using the Weather Research and
268 Forecasting (WRF) model to increasing nested spatial resolutions of 27 km, 9.5 km, 3.17 km, and finally 1.06 km
269 to account for the complex topography of the site.

270 Additionally, we worked with the air mass classification results introduced in the same work, obtained by applying
271 k-means clustering to the temporal signatures (number of back-trajectory piercings per month of the year) of
272 geographical cells on a log-polar grid (Chauvigné et al., 2019). Their method, applied to HYSPLIT back
273 trajectories between January 2011 and September 2016, yielded six prevalent clusters of air mass origin. They are
274 shown in Fig. 2 and can be shortly described as follows:

276 • Cluster C1: Northern lowlands. Air masses of Amazonian origin, which take a southward turn after
277   hitting the Andes (Graciela et al., 2011). Includes the very ASGM active "Madre de Dios" watershed.
278 • Cluster C2: Eastern/South-Eastern lowlands. Includes scrublands like the dry Chaco region between
279   Bolivia and Paraguay, but also the Pantanal wetland at the eastern frontier to Brazil.
280 • Cluster C3: Northern Chile/Southern Altiplano. Includes actively degassing volcanoes of the CVZ
281   (Tamburello et al., 2014; Tassi et al., 2011) and the La Paz valley.
282 • Cluster C4: Eastern edge of the Altiplano. Air masses passing to the east of the Titicaca lake.
283 • Cluster C5: Western altiplano. Includes the Titicaca lake, Peruvian highland, and the Pacific Ocean, also
284   passes over parts of the CVZ (Moussallam et al., 2017).
285 • Cluster C6: Cloud forest at the North-eastern edge of the Cordillera Real.

286 By following Eq. (1), Chauvigné et al. (2019) computed the relative influence of the six clusters, expressed as a
287 percentage, for each hour of the day.

288
$$P_i(t) = \frac{\sum_{k \in C_i} n_k(t) w_k}{\sum_{k \in C_n} n_k(t) w_k} \cdot 100\% \quad (1)$$

289 Where $P_i(t)$ is the relative influence of cluster i for the hour of trajectory arrival t, C_i is the set of all cells
290 assigned to cluster i, C_n is the set of all cells in the grid ($C_i \subseteq C_n$), $n_k(t)$ is the total number of pixel piercings
291 for cell k by any of the nine trajectories arriving simultaneously at CHC at hour t, and w_k is the relative weight
292 of cell k as a function of mean residence time and distance to CHC.

293   Air masses arriving at CHC are usually composed of a mix of the six clusters, and in only very few cases the
294   relative influence of one single cluster reaches 100%. Thus, we applied a selection threshold to assign hourly
295   measurements at CHC to one single cluster: If the percentage of relative cluster influence as calculated by Eq. (1)
296   exceeded the selection threshold for any of the six clusters, we considered the latter to be the "dominant cluster"
297   and assigned to it alone all measurements taken at CHC during the hour of back trajectory arrival. All data obtained
298   at arrival times for which none of the clusters was dominant were excluded from this analysis. Unless stated
299   otherwise, we chose a threshold of 70% to find a compromise between unambiguousness of air mass origin and
300   data availability, as the latter decreases rapidly with higher selection thresholds, especially for the weaker clusters
301   C2, C3, C4, and C6. In a nutshell, if the set of nine back trajectories arriving simultaneously at the station spent
302   over 70% of its time within cells assigned to one single cluster, we considered the latter to be the "dominant
303   cluster" (at a selection threshold of 70%).
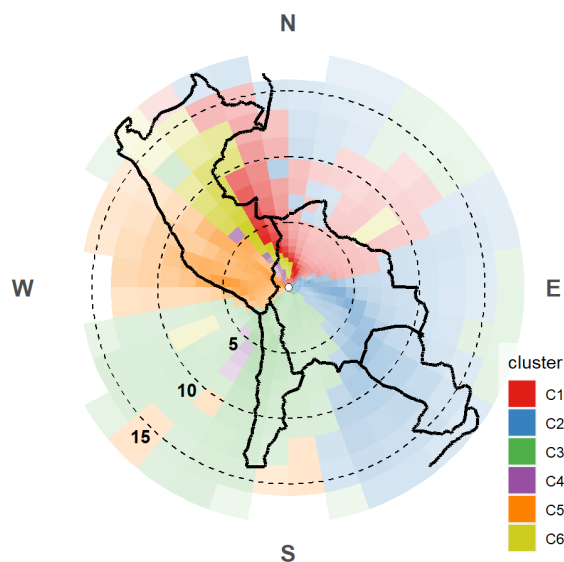
304

305   *Fig. 2: Air mass cluster definition as obtained by Chauvigné et al. (2019). Log-polar coordinate system, centered*
306   *on CHC (white dot). Cells shaded according to the square root of weight, which is a function of residence time*
307   *and distance to CHC. Distance to CHC in degrees is shown in dashed range circles. Black lines show the borders*
308   *among countries.*

309

310

311   **2.5 Pollution maps**

312   To further visualize the link between air mass origin and TGM concentrations, we produced what we call
313   "pollution maps". These are based on the same set of HYSPLIT back trajectories introduced previously, and were
314   computed with the following procedure: First, for each single back trajectory, we assigned the TGM concentration
315   at back trajectory arrival to each of its endpoints (each back trajectory consists of 96 trajectory endpoints, one for

316 every hour of its runtime). Then we defined a geographical grid and grouped together all endpoints (defined in

317 space by latitude, longitude, and elevation over ground level) falling into the same grid cell. Finally, for each grid

318 cell, we calculated the arithmetic mean of all TGM concentrations assigned to the corresponding grouped

319 endpoints.

320 It has to be highlighted that this procedure permits the multiple counting of the same measured TGM concentration

321 in the calculation of one single grid cell mean. This happens if more than one endpoint of the same trajectory or

322 endpoints of different trajectories with the same arrival time fall into the same geographical grid cell. We

323 considered this sort of inherent weighting to be desirable, as it gives greater weight to TGM concentrations

324 assigned to air masses passing an extended period of time over the grid cell in question. However, to assure a

325 certain degree of statistical significance, we excluded those grid cell means based on less than 10 independent

326 data points on TGM concentration ($n < 10$).

327 To account for growing trajectory uncertainty with increasing distance to the receptor site (CHC), avoid the

328 misinterpretation of a pollution map as a satellite image, and allow for the easy visual comparison between

329 pollution maps and air mass clusters, we used the exact same CHC centered log-polar grid as deployed in

330 Chauvigné et al. (2019).

331 With the goal of focusing on potential sources and sinks acting close to the surface, we excluded all trajectory

332 endpoints with an elevation greater than 1000 m a.g.l from this analysis (assuming an average boundary layer

333 height of 1000 m a.g.l). This means essentially that only trajectories passing at low altitudes over a grid cell have

334 an influence on the TGM average calculated for the cell.

3. Results

3.1 TGM concentrations in normal and ENSO conditions, seasonality

337 A summary of the monthly averaged TGM concentrations is presented in Fig. 3a. The data shows an overall rising

338 trend during the measurement period. As this trend exhibits a striking similarity to the evolution of the ONI index

339 (Fig. 3c), we suggest an important ENSO influence on TGM measured at CHC. This will be discussed in detail

340 in an upcoming publication. In the present paper, we labelled the last nine months of our measurement period

341 (June 2015 - Feb 2016) with ONI > 1 as ENSO conditions (EC) and excluded them from most of our analysis as

342 not representative of normal conditions (NC).

344 We obtained a mean TGM concentration of $0.89 \pm 0.01\ ng\ m^{-3}$ for NC and a significantly higher mean of

345 $1.34 \pm 0.01\ ng\ m^{-3}$ for EC ($p < 2.2 \cdot 10^{-16}$, Mann-Whitney test). For both NC and EC, we can observe a

346 similar seasonal pattern, with low TGM concentrations during the dry season, rising TGM concentrations during

347 BB season, and highest TGM concentrations at the beginning of the wet season (Fig. 3a and Fig. 3b). In the case

348 of NC, TGM concentrations started declining again in January, while this was not observable for EC.

349
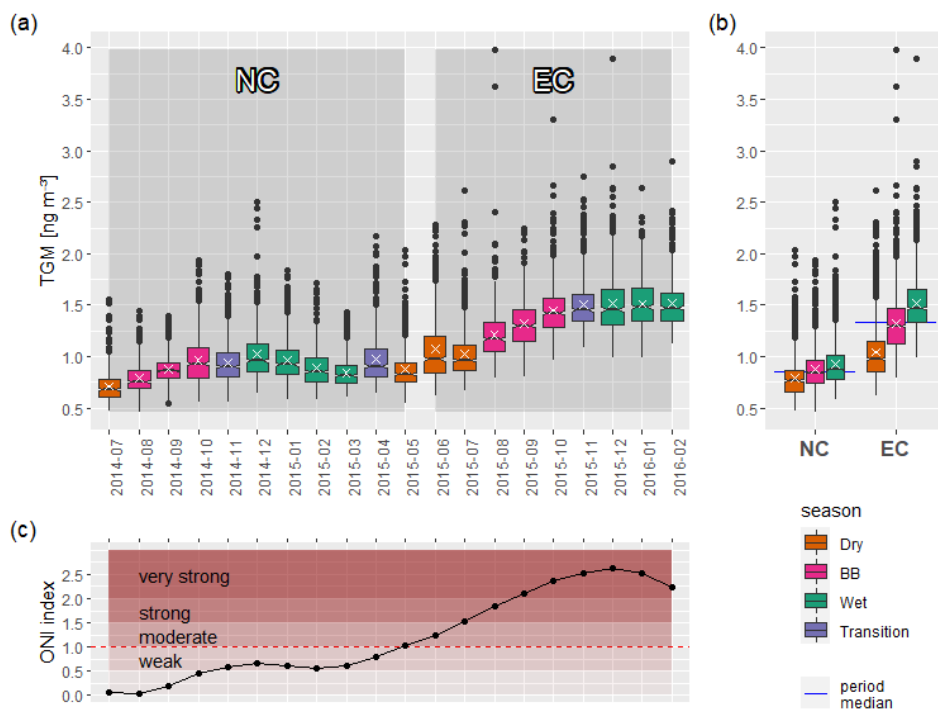
Fig. 3: (a) Time evolution of TGM at CHC during the entire measurement period. Notches display 95% confidence intervals for the median, means are shown as white crosses, "normal conditions" (NC) and "ENSO conditions" (EC) time intervals as shaded boxes. (c) Evolution of the ONI index during the same period alongside NOAA definitions on the strength of ENSO phases. The dashed red line shows the boundary value we used here to separate NC from EC (ONI = 1). (b) Seasonality of TGM in CHC during NC and EC, transition months excluded. Horizontal blue lines show the total median of the respective period.

3.2 Diel cycle, urban influence and nearby contamination

Given that the metropolitan area of La Paz/El Alto is located less than 20 km downhill of the measurement site, we investigated the possibility of a statistically important urban influence on TGM measurements. Previous studies (Andrade et al., 2015, Wiedensohler et al., 2018) have shown a significant influence of regional sources and the nearby metropolitan area on CO and eBC concentrations measured at the station. A marked increase in average CO and eBC diel patterns (Fig. 4b and Fig. 4c), starting at around 9:00 local time, has been linked to the arrival of the Altiplanic planetary boundary layer, vehicle traffic, and urban contamination in general. In contrast, the diel cycle of TGM (Fig. 4a) is qualitatively different, with no marked increase associated to the arrival of the boundary layer, but instead slightly lower TGM values between about 7:00 and 19:00 local time, which coincides well with the typical hours of sunlight and generally boundary layer influence. The absence of a diel pattern driven by traffic and urban pollution is not very surprising, since there are no major sources of mercury in the poorly industrialized cities of La Paz and El Alto, and domestic heating is nearly absent. The only potential local sources we suggest could be the occasional waste burning by individuals and a cement factory located at about 40 km to

370 the southwest of the station (Cemento Soboce, 16°38'49.2"S 68°19'01.2"W, Fig. 1). Either way, the magnitude of

371 urban or traffic-related TGM contamination at CHC appears to be negligible.

372 Still, one event where TGM concentrations were clearly driven by nearby anthropogenic pollution was Saint

373 John's Eve, the night between the 23rd and 24th of June 2015, where TGM concentrations peaked alongside CO

374 and eBC concentrations (Fig. 4d, Fig. 4e, Fig.4f). During nights around that traditional festivity, numerous

375 bonfires are lit and fireworks are launched in the region. In the bonfires, not only untreated wood is used for

376 combustion, but also garbage, old furniture, and other objects. The relatively high mean TGM concentrations

377 during June 2015, as compared to May and July 2015 (Fig. 3a), could be explained by the Saint John event alone,

378 especially if we consider the relatively poor data coverage during that month (only 21 out of 30 daily averages

379 available) and the resulting greater weight given to a few days (~ 6 days) of elevated concentrations.
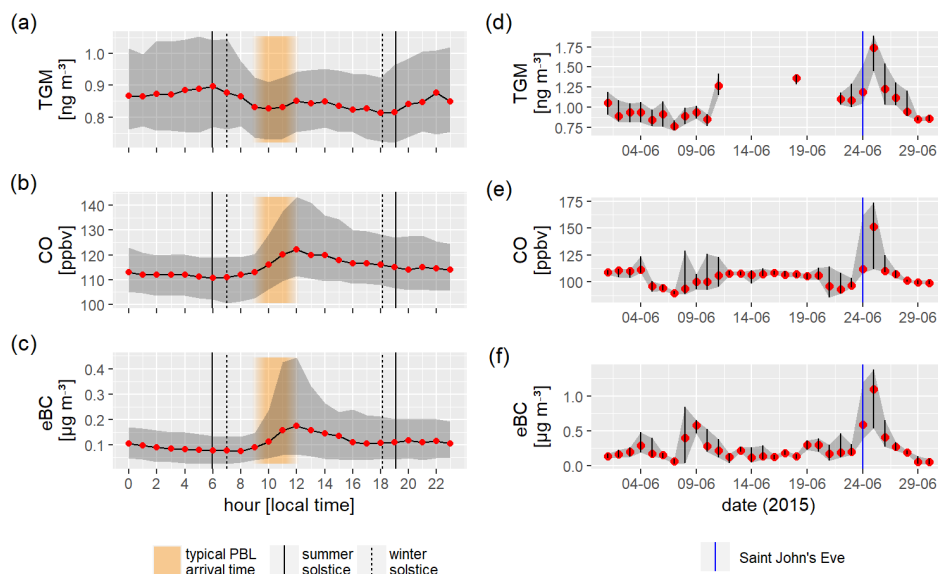
380

381 *Fig. 4, Left: Median diel cycles of (a) TGM, (b) CO, and (c) eBC for NC. Limits of grey shaded area correspond*

382 *to the 25th and 75th percentile. Vertical lines represent sunrise and sunset hours for the summer solstice in the*

383 *wet season (solid line) and the winter solstice in the dry season (dashed line). The typical arrival time of the*

384 *urban-influenced Altiplanic planetary boundary layer (PBL) is highlighted in orange. Right: Daily averaged (25th*

385 *percentile, median, 75th percentile) (d) TGM, (e) CO, and (f) eBC during June 2015.*

386   **3.3 Spatial differences of TGM concentrations, air mass origin**

387 The evident seasonal pattern in transportation pathways towards CHC is visualized in Fig. 5. The most important

388 air mass clusters during NC, measured by mean relative influence and appearance as the dominant cluster, were

389 Amazonian C1 and Altiplanic C5 (Fig. 5c and Fig. 5d).

390 In the dry season, most of the air masses arriving at the station were western Altiplanic (C5), passing over the

391 Peruvian highlands and the Titicaca lake. This changed in the wet season with a clear shift towards predominantly

392 Amazonian/lowland air masses (northerly C1 and easterly C2). The Altiplanic cluster C5 was weak during that

393 time of the year (mean relative influence < 10%).

394 With much less seasonal variation, southerly Altiplanic air (Cluster C3) arrived occasionally from the border

395 between Bolivia and Chile after passing through parts of the CVZ and - frequently - the urban area of La Paz/El

396 Alto. Altiplano/lowland interface clusters C4 and C6 were relatively weak throughout the year and appeared very

397 infrequently as dominant clusters at a threshold of 70% (Fig. 5d).

398 As shown in Fig. 6, we tried to infer potential source and sink regions of TGM through clustering results and a

399 pollution map (based on an endpoint cutoff altitude of 1000 m a.g.l, as described in the methodology section;

400 pollution map results at different cutoff altitudes can be consulted in Appendix B). Based on all NC data, Northern

401 Amazonian and Southern Altiplanic air masses, especially those passing over or close to reportedly degassing

402 volcanoes south of CHC (Ollague, San Pedro, Putana, Lascar, Lastarria; Tamburello et al., 2014; Tassi et al.,

403 2011), carried the highest mean TGM concentrations (around $0.94 \pm 0.02\ ng\ m^{-3}$ and $1.08 \pm 0.08\ ng\ m^{-3}$

404 respectively), while western Altiplanic and south-eastern lowland air masses showed the lowest mean TGM

405 concentrations (around $0.80\ \pm 0.02\ ng\ m^{-3}$ and $0.85\ \pm 0.02\ ng\ m^{-3}$ respectively, Fig. 6a). By grouping data

406 by season (i.e. wet, dry, and BB), more detailed information could be extracted (Fig. 6b). Only the Northern –

407 Amazonian cluster C1 showed both the highest CO and TGM concentrations during the BB season (means of

408 $150 \pm 5\ ppbv$ and $0.99 \pm 0.04\ ng\ m^{-3}$ respectively). Western Altiplanic cluster C5 exhibited the lowest

409 mean TGM concentrations in the dry season ($0.77 \pm 0.01\ ng\ m^{-3}$) and the highest TGM concentrations in the

410 wet season ($0.93 \pm 0.07\ ng\ m^{-3}$). The mean concentration in southern-Altiplanic cluster C3 was $0.92 \pm$

411 $0.05\ ng\ m^{-3}$ with no significant differences between the wet and BB season ($p = 0.76$, Mann-Whitney test).

412 Eastern lowland cluster C2 did only contribute as a dominant cluster during the wet season, but showed by far the

413 lowest mean TGM concentrations during that time of the year ($0.82 \pm 0.02\ ng\ m^{-3}$). The seasonal change in

414 transport pathways becomes evident if we consider that in the dry season, only Altiplanic C5 contributed

415 significantly as a dominant cluster (at a selection threshold of 70%). No useful information could be extracted

416 about altiplano-lowland interface clusters C4 and C6, as their relative influence throughout the year was low (Fig.

417 5c and Fig.5d).

418

419
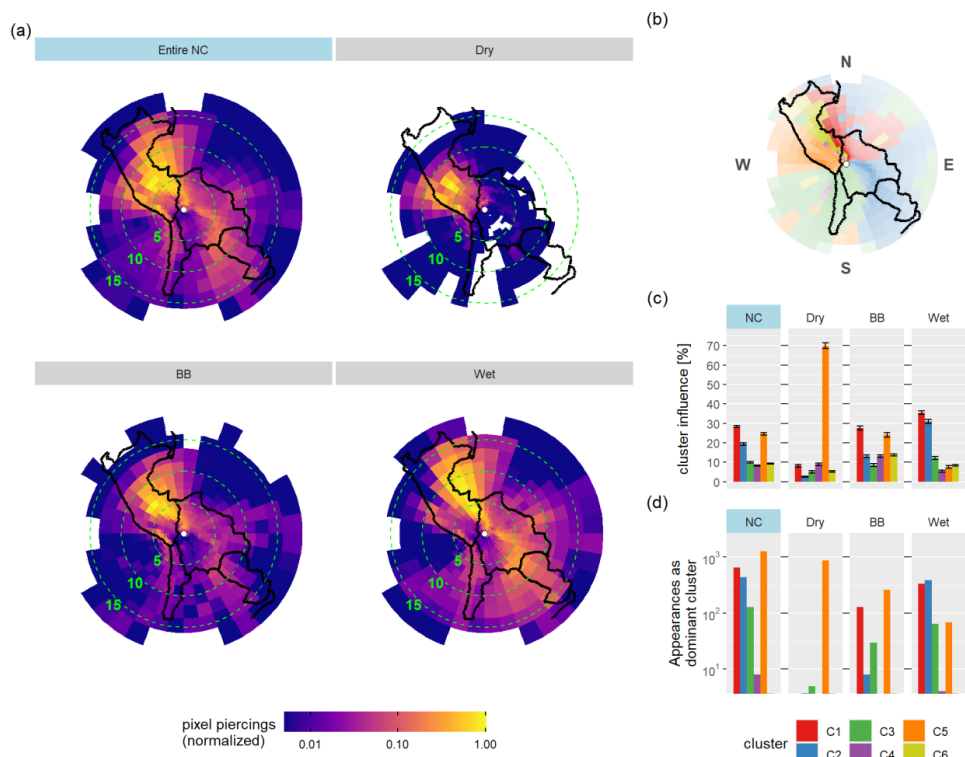
Fig. 5: (a) Total number of back trajectory piercings per pixel for NC and its seasons, normalized through division
by the maximum, so that "1" corresponds to the most frequently pierced pixel. Note the logarithmic color scale.
The polar grid has constant angular, but variable radial resolution and is centered on CHC (white dot). Distance
to CHC in degrees is shown in dashed circles. Right: (b) Reminder of the cluster definition as obtained by
Chauvigné et al. (2019), using the same polar grid. (c) Weighted mean relative influence (%) for the six clusters
during the entire NC and its seasons. (d) Number of cluster appearances as "dominant cluster" at a threshold of
70%. Note the logarithmic y-axis.

427
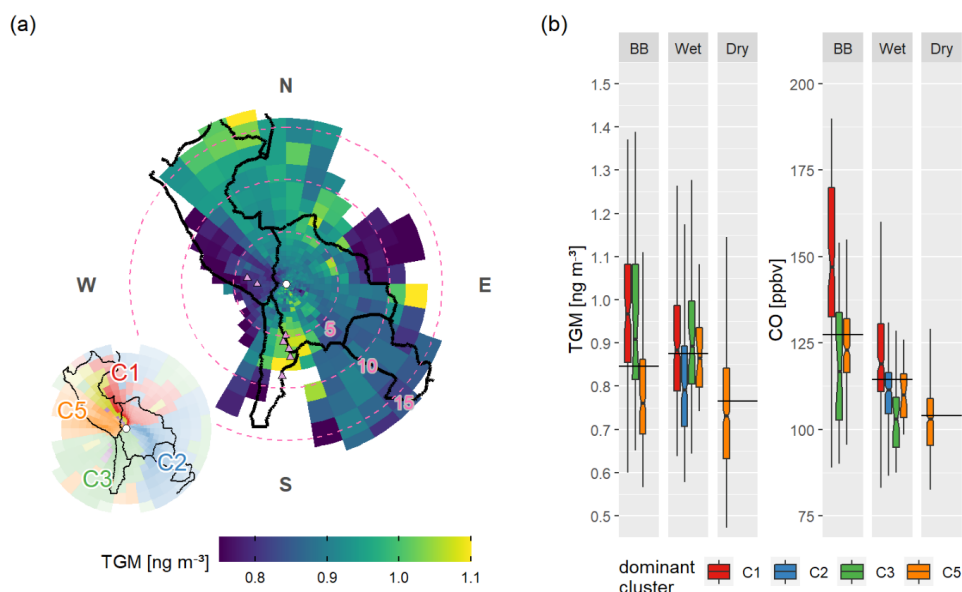
Fig. 6: (a) Pollution map based on TGM data taken during the entire NC. Polar grid is centered on CHC (white dot). Distance to CHC in degrees is shown in dashed range circles. Trajectory endpoints with an elevation > 1000 m a.g.l. and cells with less than 10 data points (n < 10) were excluded. Color scale capped at the limits. Pink triangles show selected degassing volcanoes in the CVZ, from north to south: Sabancaya, Ubinas, Ollague, San Pedro, Putana, Lascar, Lastarria. The small map shows the air mass cluster definition. (b) TGM and CO concentrations for different seasons and clusters during NC, based on a cluster selection threshold of 70%. Outliers and groups with n < 10 are not shown in the plot. Horizontal lines show seasonal medians based on all NC data.

436

4. Discussion

4.1 TGM means and seasonality

TGM concentrations during NC (11-month mean from July 2014 to May 2015: $0.89 \pm 0.01\ ng\ m^{-3}$) were about 10% to 15% lower, compared to subtropical sites of the Southern Hemisphere such as Amsterdam Island in the remote southern Indian Ocean (37.7983 S - 77.5378 E, 55 m a.s.l) with a GEM annual mean of $1.034 \pm 0.087\ ng\ m^{-3}$ (from 2012 to 2017; Slemr et al. 2020) and the Cape Point GAW station in South Africa (34.3523 S - 18.4891 E, 230 m a.s.l) with a GEM annual mean around $1\ ng\ m^{-3}$ (from 2007 to 2017; Martin et al., 2017; Slemr et al., 2020). No GEM annual mean below $1\ ng\ m^{-3}$ was observed in these two atmospheric mercury monitoring stations in 2014 and 2015, corresponding to the CHC NC period. Mean annual GEM concentrations of $0.95 \pm 0.12\ ng\ m^{-3}$, i.e. close but still higher than the NC TGM concentrations, were observed from 2014 to 2016 (Howard et al., 2017) at the Australian Tropical Atmospheric Research Station (ATARS) in Northern Australia (12.2491 S - 131.0447 E, near sea level) while the mid-latitude Southern Hemisphere site of global GAW Cape Grim (40.683 S – 144.689 E, 94 m a.s.l) exhibited annual mean concentrations around $0.86\ ng\ m^{-3}$

450 (from 2012 to 2013; Slemr et al., 2015). TGM concentrations at CHC are well in line with measurements on the

451 continent performed at Titicaca lake, at around 3800 m a.s.l and about 60 km west from our site (not continuously

452 measured between 2013 and 2016: TGM mean of $0.82 \pm 0.20 \, ng \, m^{-3}$ in the dry and $1.11 \pm 0.23 \, ng \, m^{-3}$ in the

453 wet season; Guédron et al., 2017) and in Patagonia (from 2012 to 2017, GEM mean of $0.86 \pm 0.16 \, ng \, m^{-3}$,

454 Dieguez et al., 2019).

455 CHC TGM during NC showed a marked seasonality, with lowest TGM during the dry season ($0.79 \pm$

456 $0.01 \, ng \, m^{-3}$), increasing values during BB season ($0.88 \pm 0.01 \, ng \, m^{-3}$) and highest TGM during the wet

457 season ($0.92 \pm 0.01 \, ng \, m^{-3}$). This behaviour is congruent with the results from Guedrón et al. (2017), even

458 though the seasonal difference did not appear statistically significant for the latter. The marked seasonality at the

459 CHC site is in contrast to what has been observed at some subtropical and mid-latitude sites in the Southern

460 Hemisphere, both in terms of the amplitude and the seasonal average level (Howard et al., 2017; Slemr et al.,

461 2015, 2020).

462 This seasonality is likely a product of the superposition of several important drivers, coupled with seasonal

463 changes in transportation pathways (Fig. 5). In the next sections, we further explore the potential role of BB related

464 Hg emissions, the Amazon rainforest, and the Pacific Ocean. We also explore volcanoes in the CVZ and ASGM

465 as atmospheric Hg sources without specific seasonality but with possible influence on CHC TGM levels.

466

467 **4.2 Biomass burning and TGM/CO emission ratio**

468 **4.2.1 Biomass burning influence**

469 BB is an important source of atmospheric mercury (Obrist et al., 2018; Shi et al., 2019). Friedli et al. (2009)

470 estimated global mercury emissions from BB and found a high contribution from South America ($13 \pm$

471 $10 \, Mg_{Hg} \, yr^{-1}$ for its northern hemispheric and $95 \pm 39 \, Mg_{Hg} \, yr^{-1}$ for its southern hemispheric part).

472 Michelazzo et al. (2010) measured Hg stored in Amazonian vegetation before and after fires, finding that mercury

473 emissions originated mostly from the volatilization of aboveground vegetation and the plant litter layer (O-

474 horizon). Very recently Shi et al. (2019) showed, among others, high Hg emissions in northern Bolivia, a region

475 overlapping very well with the source region of Amazonian cluster C1. Indeed, for this cluster, whose BB

476 influence was already confirmed by Chauvigné et al. (2019), we found both the highest CO and TGM

477 concentrations during the BB season (compare to Fig. 6b and Fig. A1), in both cases significantly higher than

478 during the rest of the NC ($p < 2.2 \cdot 10^{-16}$ and $p < 0.0008$ respectively, Mann-Whitney test).

479

480 In order to further explore the link between BB and TGM in our data, independently of computed HYSPLIT back

481 trajectories, we used the combination of in situ measured CO and eBC data as tracers for distinct combustion

482 sources and transport times (Choi et al., 2020; Subramanian et al., 2010; Zhu et al., 2019). We grouped CO and

483 eBC data into eight percentile groups each, ranging from 0th to 100th in steps of 12.5% (CO range: $37 \rightarrow$

484 $336 \, ppbv$; eBC range: $0 \rightarrow 5.09 \, \mu g \, m^{-3}$). Based on these groups we produced an 8x8 grid, where each cell

485 ("pollution signature") corresponds to a combination of CO and eBC concentration intervals. We then calculated

486 the median TGM concentration for each pollution signature in the grid (Fig. 7a).

487

488 Pollution signatures showed a clear seasonal trend. During the dry season, eBC was tendentially high and CO
489 low. TGM concentrations tended to increase with rising CO concentrations, while even highly eBC enriched air
490 masses had very low TGM concentrations in the absence of CO (for example, cells B-8, C-8). The latter suggests
491 that urban pollution originating from traffic does not act as an important driver of atmospheric Hg measured at
492 CHC, in agreement with the TGM diel pattern (Fig. 4a), which shows no TGM increase upon arrival of the
493 frequently traffic influenced planetary boundary layer and a simultaneous increase in eBC. During the wet season,
494 eBC at CHC station was tendentially very low, which is likely linked to the increased wet deposition of particulate
495 matter during that season, while CO concentrations were very variable. The absence of a visible pattern concerning
496 TGM in those pollution signatures suggests that TGM concentrations during the wet season are either not
497 importantly affected by combustion of any kind, or that around this time different combustion sources are
498 indistinguishable through their eBC and CO signatures.

499

500 Finally, BB season pollution signatures generally showed very high CO and highly variable eBC concentrations.
501 Within those signatures, TGM concentrations clearly increased with rising CO concentrations but did not depend
502 strongly on eBC loadings, even though they tended to be lower in the case of very low eBC (example: H1, H3,
503 G3, F3. Exception: H2).
504 Considering that atmospheric lifetime is much shorter for BC than for CO (days - weeks for BC, Cape et al., 2012;
505 Park et al., 2005; months for CO, Khalil et al., 1990), especially under conditions of high wet deposition, we can
506 expect that even if both eBC and CO are strongly co-emitted during BB events, air masses arriving at CHC should
507 be significantly enriched in CO only after a few days of transport. We can thus interpret the steadily high CO but
508 comparatively low eBC loading of air masses with these pollution signatures as the result of an important BC
509 deposition (wet and dry) during the transport between pollutant source and receptor side regions, either due to
510 precipitation favoring wet deposition or a transport time of at least a few days. As the metropolitan area of La
511 Paz/El Alto, a hotspot for BC (Wiedensohler et al., 2018), is quite close to the station (< 20 km) and transport
512 time is therefore usually less than a few hours (compare to Fig. C1 in Appendix C), we can exclude urban
513 influences as contributors to these pollution signatures and assign them to BB.

514

515 As median TGM concentrations were significantly higher in those pollution signatures occurring almost
516 exclusively in the BB season (over 85% of the time, Fig. 7a), compared to median NC concentrations
517 ($0.93 \, ng \, m^{-3}$ vs. $0.85 \, ng \, m^{-3}$, $p = 1.7 \cdot 10^{-11}$, Mann-Whitney test), we can conclude that there is an
518 important influence of regional and continental BB on atmospheric mercury concentrations in the Bolivian Andes.
519 This occurs only during a few months of the year (August - October) and it is mostly constrained to northern-
520 Amazonian air masses (cluster C1, remotely obtained CO concentrations in the cluster C1 source region are shown
521 in Appendix A).

522
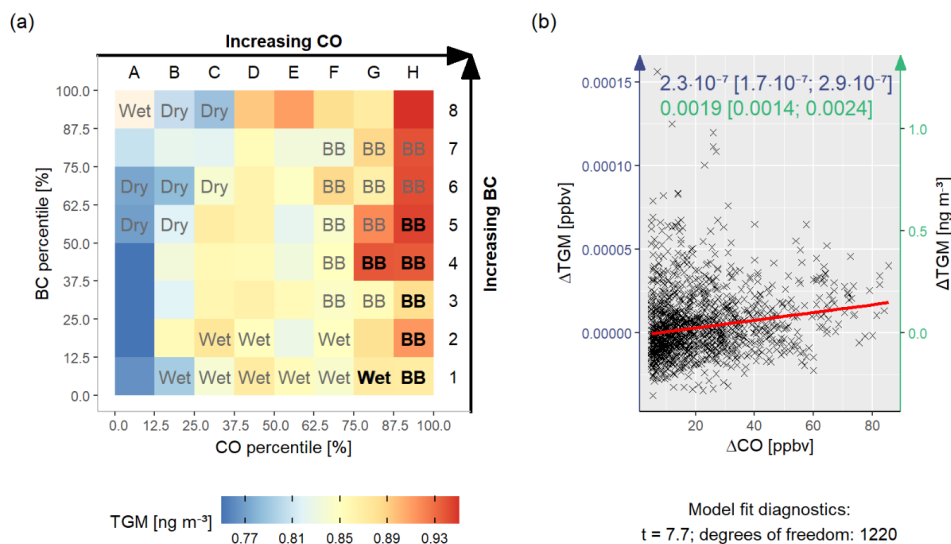
Fig. 7: (a) TGM medians for different combinations ("pollution signatures") of eBC and CO concentrations, each
split into 8 percentile groups ranging from 0 to 100%, so that the first group contains data below the 12.5th and
the last group data above the 87.5th percentile. All data were taken during NC at CHC. Grey (black) letters mark
signatures whose data falls into the respective season more than 51% (85%) of the time. Cells with n <30 shaded
out proportionally. Color scale centered on NC median and capped at the limits. (b) Red line shows robust linear
model (iteratively reweighted least squares) between ΔTGM and ΔCO, defined as the difference between actual
measurement and assumed background concentrations, for all data in pollution signatures with a >51%
occurrence during NC BB season (all cells with grey or black "BB" letters in (a)). The resulting slope, which can
be interpreted as TGM/CO emission ratio, is given in units of $ppbv_{TGM}\ ppbv_{CO}^{-1}$ (blue) and
$(ng\ m^{-3})_{TGM}\ ppbv_{CO}^{-1}$ (green) with its 95% confidence interval.

533

4.2.2 TGM/CO emission ratio

Having established a clear link between TGM and long-range transported BB in our data, we aimed to estimate
an average biomass burning TGM/CO emission ratio on the continent. A first obstacle arises from the fact that
BB is not the only source for TGM and CO measured at Chacaltaya. CO in particular is also readily emitted by
anthropogenic activities (e.g. urban, traffic) in the surrounding Altiplano, as can be inferred from CO diel patterns
(Fig. 4b) and previous work (Wiedensohler et al., 2018). In consequence, simply computing TGM vs. CO in the
entire unfiltered CHC dataset would not provide the biomass burning related TGM/CO emission ratio, but a sort
of "net emission ratio" over different sources of pollution with distinct emission ratios. To remove this distorting
factor as much as possible and obtain a "best guess" biomass burning TGM/CO emission ratio, we used the results
from the previous section ("pollution signatures"): We attempted to isolate highly BB influenced air masses by
selecting only data with pollution signatures occurring preferentially during the BB season (> 51% of signature
data taken in BB season, Fig.7, left) as BB representatives.

546   With this data selection performed, a linear model between TGM and CO could not yet be computed directly to

547   obtain the emission ratio, as this would assume constant TGM and CO background conditions for the whole data

548   selection. This is not a valid assumption, considering that the selection contains TGM data from different months

549   and that a strong seasonal pattern was observed (Fig. 3a and Fig. 3b). To account for the changing background

550   conditions, we first computed ΔTGM and ΔCO, which we defined as their measured concentration minus their

551   assumed background concentration at the time of measurement. We expressed the TGM background through a

552   30-days running median, as it is clearly not constant during the year and seasonally shifting concentrations cannot

553   be attributed to BB only. This is different for CO, where we can assume that BB is the main driver of the seasonal

554   signal in South America (Fig. A1a) and that the BB-unrelated fluctuations in background concentrations are small

555   in comparison to the BB induced variations in measured concentrations at CHC (Fig. A1b). We thus used a simple

556   median using all NC data to express the CO background (Illustrated in Fig. A1b).

557   Finally, we determined the TGM/CO emission ratio through the use of a robust linear regression (linear regression

558   with iterative reweighting of points) between ΔTGM and ΔCO ($\Delta TGM = a + b \cdot \Delta CO$), obtaining a slope of

559    $(2.3 \pm 0.6) \cdot 10^{-7} ppbv_{TGM} \, ppbv_{CO}^{-1}$ (Fig. 7b). This obtained emission ratio is robust towards changes in

560   the parameters chosen for its calculation (Sensitivity analysis presented in Appendix D), and is in good agreement

561   with previous results. Ebinghaus et al. (2007) deduced TGM/CO emission ratios of $(1.2 \pm 0.2) \cdot$

562    $10^{-7} \, ppbv_{TGM} \, ppbv_{CO}^{-1}$ and $(2.4 \pm 1) \cdot 10^{-7} \, ppbv_{TGM} \, ppbv_{CO}^{-1}$ during CARIBIC flights over Brazil

563   through measurements performed directly within fire plumes. Penzias et al. (2007), using a more similar approach

564   to ours, obtained results ranging from $(1.6 \pm 1) \cdot 10^{-7} \, ppbv_{TGM} \, ppbv_{CO}^{-1}$ for air massing originating in

565   Pacific Northwest US up to $(5.6 \pm 1.6) \cdot 10^{-7} \, ppbv_{TGM} \, ppbv_{CO}^{-1}$ for those originating in industrial East

566   Asia (*numbers converted from* $(ng \, m^{-3})_{TGM} \, ppbv_{CO}^{-1} \, to \, ppbv_{TGM} \, ppbv_{CO}^{-1}$).

567   We observe a high scatter around our regression line of best fit, which is not surprising, considering the distance

568   from the receptor site to the source region and the resulting dilution and mixing. Due to that, our data pairs of

569   TGM and CO do not correspond to the emissions of one single fire event, but many different fires and plumes and

570   also distinct times and conditions of aging. The obtained emission ratio should thus be interpreted as an average

571   emission ratio of all fires in the northern Bolivian lowlands and the Amazon, after some aging has occurred.

572   ### 4.3 The potential role of the vegetation in the TGM cycle

573   Globally, the role of vegetation in the mercury cycle is not yet completely understood, but there is much evidence

574   pointing towards both reactive mercury (RM) deposition on leaf surface and a direct vegetation uptake of GEM.

575   However, as highlighted in the literature review by Obrist et al. (2018), these pathways, especially the latter, are

576   still not well constrained. Recently, Jiskra et al. (2018), reported a significant correlation between the remotely

577   sensed vegetation tracer NDVI (normalized difference vegetation index) and GEM levels for individual sites in

578   the Northern Hemisphere and argued that the absence or weakness of Hg seasonality in many sites of the Southern

579   Hemisphere might be linked to its comparatively lower landmass and lesser vegetation uptake. A similar point

580   was made earlier by Obrist (2007), who proposed that vegetation uptake in the Northern Hemisphere might be

581   partly responsible for the observed TGM seasonality in Mace Head, Ireland, a hypothesis based on the correlating

582   seasonal patterns of atmospheric TGM and CO_2. Indeed, Eriksen et al. (2002) showed in mesocosm experiments

583   that foliar Hg concentrations in gas chambers increase over time, levelling off after 2-3 months. They furthermore

584   reported that roughly 80% of the total accumulated Hg was stored in leaf matter and that soil Hg levels in the

585   mesocosms had no significant effect on foliar Hg concentration, a piece of strong evidence that Hg is taken up

586   directly from the atmosphere and not from the soil. Some very similar points were made by Grigal (2003), based

587   on a review of Hg concentrations in forest floors and forest vegetation. Although it is assumed that vegetation acts

588   as a net sink for atmospheric mercury (Obrist et al., 2018), Yuan et al. (2019) studied mercury fluxes in a

589   subtropical evergreen forest and found isotopic evidence for a GEM re-emission process within leaves,

590   counteracting partly the GEM uptake. They also reported a strong seasonality in mercury fluxes, with the highest

591   GEM uptake in the growing / wet season. Considering these previous results, a modulation of continental-wide

592   Hg levels through the Amazon rainforest is likely. Indeed, Figueiredo et al. (2018) already suggested that the

593   Amazon rainforest acts as a net sink for atmospheric mercury, based on forest soil profiles.

594   To address such a possible link between TGM and vegetation in our data, we focused on lowland air masses only,

595   as vegetation coverage in the altiplano is sparse, GPP is low and consequently no important vegetation sink effect

596   is to be expected in Altiplanic air masses. Although both clusters C1 and C2 would qualify as lowland clusters

597   passing over evergreen forests, C2 did not provide enough data to compute a useful series of monthly averages.

598   Therefore, we selected Amazonian cluster C1 as the sole representative of Amazonian air masses. We explored

599   two different proxies for a possible vegetation sink effect: CO_2 concentrations measured at CHC (detrended,

600   assuming a Southern Hemisphere linear trend of 2 ppm/year; trend based on AIRS CO_2 data between January

601   2010 and January 2015, averaged over whole South America) and satellite obtained solar induced fluorescence

602   (SIFTER) averaged over the (legal) Amazon rainforest as a proxy for amazon GPP. We then computed the slope

603   of robust linear models for the combinations TGM vs. CO_2 $(TGM = a + b \cdot CO_2)$ and TGM vs. SIFTER

604    $(TGM = a + b \cdot SIFTER)$ for C1 dominant air masses at increasing selection thresholds.

605   We observe an interesting trend, where the magnitude of the slopes becomes more important and slope uncertainty

606   (compare to Sect. 2.2.6, "Uncertainties and confidence intervals") decreases with an increasing Amazonian cluster

607   C1 selection threshold (Fig. 8a and Fig. 8b). For thresholds of 70% and 80%, the resulting TGM vs. CO_2 slopes

608   are 0.047 [0.035; 0.060] and 0.058 [0.041; 0.075] $(ng\ m^{-3})_{TGM}\ ppm_{CO2}^{-1}$ respectively, while the

609   resulting   TGM   vs.   SIFTER   slopes   are $-0.82\ [-1,11; -0.53]$ and

610    $-1.51\ [-2.05; -0.97]\ (ng\ m^{-3})_{TGM}\ (mW\ sr^{-1}m^{-2}nm^{-1})_{SIF}^{-1}$. Closer inspection of the corresponding

611   TGM, CO_2, and SIFTER monthly averages at a C1 threshold of 70% visualizes how both TGM and CO_2 reached

612   their minimum in March 2015, coinciding with a peak of Amazon SIFTER as a proxy for Amazon GPP (Fig. 8d,

613   Fig. 8e, Fig. 8f).

614
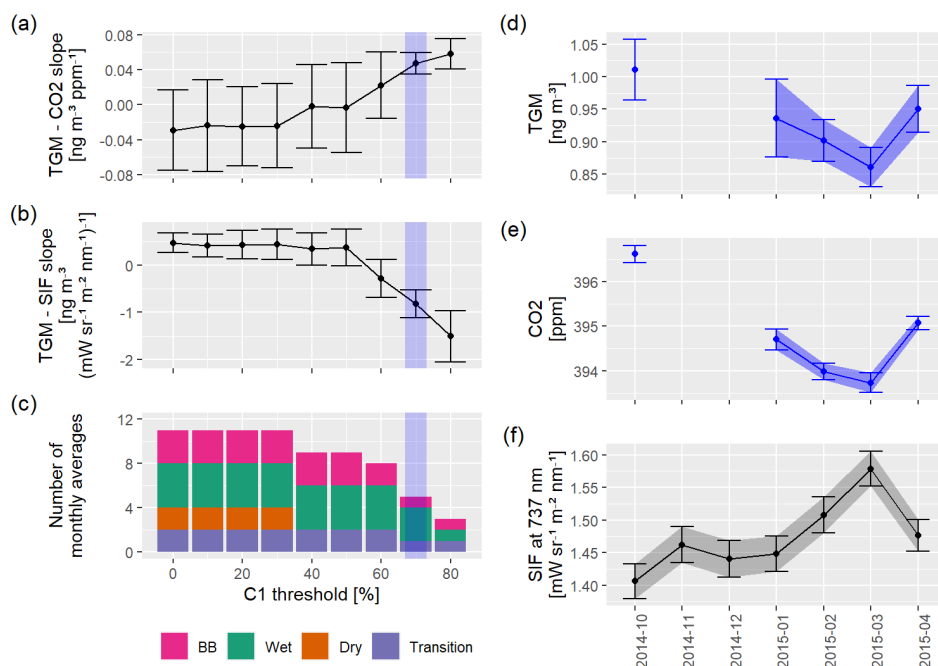
Fig. 8: Left: Slopes for (a) TGM vs. CO_2 ($TGM = a + b \cdot CO_2$) and (b) TGM vs. SIFTER ($TGM = a + b \cdot SIFTER$) for robust linear models based on monthly averages, as a function of the chosen Amazonian cluster C1 threshold and the resulting selection of data. TGM and CO_2 monthly averages based on less than 30 data points (n < 30) were excluded. Error bars show 95% confidence interval. Threshold used for the right-hand side of the plot (C1 mean influence > 70%) shaded in blue. (c) Number of monthly averages available for the linear models at the respective threshold, excluding all monthly averages with n < 30. Color shows the partition over the seasons. Right side: Example of the time series of monthly averages for (d) TGM, (e) CO_2, and (f) SIFTER at a C1 selection threshold of 70%. TGM and CO_2 reach their minimum when amazon SIFTER peaks.

These results provide arguments for the presence of a vegetation-related Hg sink in Amazonian air masses, mainly during the wet season. As to be expected from the comparatively low vegetation coverage in the Altiplano, no such correlation with CO_2 or SIFTER was found for air masses of Altiplanic origin. A clear downside to our approach here is that higher selection thresholds for C1, and thus a cleaner selection of northern Amazonian air masses, provide a smaller number of monthly averages available for the linear models (Fig. 8c). Due to the seasonality of transport pathways towards the station (Fig. 5), the available monthly averages of C1 dominated air masses are not equally distributed over the year, but fall mainly into the wet season. As these C1 dominated air masses fall very rarely into the dry season, we cannot make any assumptions about the relationship between TGM and vegetation tracers in lowland air masses during that time of the year.

Concerning our second vegetation proxy, remotely sensed SIFTER averaged over the Amazon rainforest, we have to emphasize the difficulty in linking satellite obtained data with in situ single measurements at CHC, which can

Atmospheric
Chemistry
and Physics
Discussions

Open Access

EGU

634   only be done under strong assumptions. We chose the whole legal Amazon as a bounding box under the hypothesis

635   that it is, on average, representative of the vegetation that Amazonian C1 dominant air masses are subject to,

636   before arriving at CHC. We further assumed that the average transport time between the Amazon and CHC station

637   is much shorter than one month, so that no lag has to be introduced between monthly averaged satellite and in situ

638   observations (compare to typical transport times shown in Appendix C). Considering these assumptions, our

639   results have to be taken with care, especially as the seasonality of transport pathways does not allow us to discern

640   if the Amazon rainforest would act as a net sink during the entire year, or only as a temporary sink during seasons

641   of high vegetation uptake. Still, the deduced TGM/CO_2 slope at cluster C1 threshold of 80% could be interpreted

642   as our best guess "TGM/CO_2 *uptake ratio*" and be used to constrain the atmospheric mercury uptake by the

643   Amazon rainforest.

644

645   **4.4 The role of the Pacific Ocean?**

646   Oceanic evasion is a major driver of atmospheric Hg concentrations (Horowitz et al., 2017; Obrist et al., 2018).

647   Especially surface waters of tropical oceans are enriched in mercury, possibly due to enhanced Hg divalent species

648   wet deposition (Horowitz et al., 2017). Soerensen et al. (2014) found anomalously high surface water Hg

649   concentrations and GEM fluxes towards the atmosphere in ocean waters within the Inter-Tropical Convergence

650   Zone (ITCZ). They explained this finding with deep convection and increased Hg divalent species deposition.

651   Floreani et al. (2018) deployed floating flux chambers in the Adriatic Sea and found the highest ocean-atmosphere

652   Hg fluxes in summer, coinciding with increased sea surface temperature (SST) and solar radiation. A similar

653   positive link between SST and atmospheric GEM concentrations was established for Mauna Loa by Carbone et

654   al. (2016).

655   In our dataset, mean TGM concentrations in western-Altiplanic air masses (C5 relative influence > 70%) were

656   significantly higher during the wet season/summer than during the dry season/winter ($0.93 \pm 0.07 \, ng \, m^{-3}$ vs.

657    $0.77 \pm 0.01 \, ng \, m^{-3}$, $p = 6.65 \cdot 10^{-7}$, Mann-Whitney test), in very good agreement with previous

658   measurements at the Titicaca lake (Guédron et al., 2017). Due to sparse vegetation coverage for cells of that

659   cluster, we can mostly exclude a seasonal influence of vegetation, and anthropogenic influences can be considered

660   unlikely candidates to introduce this sort of seasonal variation considering the low population density and the

661   infrequent use of domestic heating and cooling. To further explore possible causes, we computed the TGM

662   difference between the wet season and the rest of NC as a pollution map and found that air masses originating

663   close to the pacific coast showed much higher TGM concentrations in the wet season (austral summer), compared

664   to the rest of NC (Fig. 9). The opposite was observable for continental air masses, which is likely linked to the

665   possible presence of a vegetation sink effect, as discussed earlier.

666   Thus, we hypothesize that changing emission patterns over the Eastern Pacific Ocean might play a role in the

667   seasonal pattern of atmospheric mercury in the Bolivian Andes. Increased Hg emissions during the wet season

668   (austral summer) might be linked to an increase in SST and/or the southwards shift of the ITCZ and enhanced

669   convection over the southern Pacific Ocean.

670
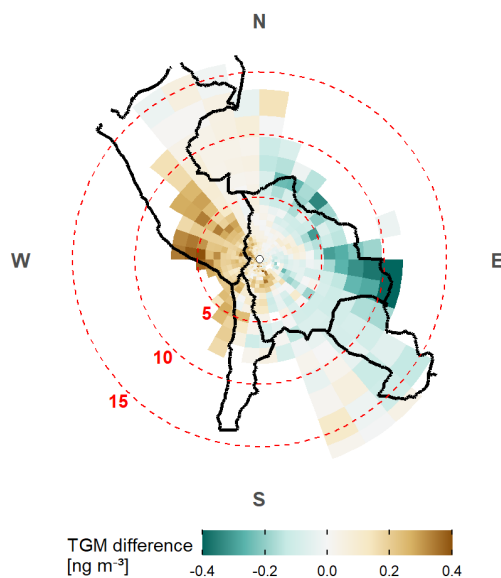
Fig. 9: Pollution map for the wet season (austral summer) minus pollution map for the rest of NC. Polar grid is

centered on CHC (white dot). Distance to CHC in degrees is shown in dashed circles. Trajectory endpoints with

an elevation > 1000 m a.g.l. and cells with less than 10 data points (n < 10) were excluded. Color scale capped

at the limits.

4.5 Volcanic influences

Previous studies have reported volcanic degassing in the CVZ, both south of CHC (Tamburello et al., 2014; Tassi

et al., 2011) and west of CHC (Moussallam et al., 2017). While to our knowledge mercury emissions or

atmospheric mercury concentrations have not yet been investigated in the CVZ, a very recent work inferred from

mercury concentrations in lichen that volcanoes in the Southern Volcanic Zone (southwards of the CVZ) can be

sources of atmospheric mercury (Perez Catán et al., 2020). As similar gas plume compositions (CO_2/S_{TOT},

S_{TOT}/HCl) were measured in volcanic emissions from the CVZ and the Southern Volcanic Zone (Tamburello et

al., 2014), we can hypothesize that volcanoes in both active regions also emit mercury in a similar fashion.

That being said, our data gives ambivalent information about the importance of a volcanic Hg source in the region.

On one hand, we found elevated mean TGM concentrations of above $1.08\ ng\ m^{-3}$ ($\pm\ 0.08\ ng\ m^{-3}$) in air

masses passing at low altitudes (under 1000 m a.g.l) over the south-western frontier between Bolivia and Chile,

the same regions of the CVZ where Tassi et al. (2011) and Tamburello et al. (2014) reported important volcanic

degassing (Fig. 6a). Southern-Altiplanic cluster C3 in comparison, which represents best the general origin of

similar air masses, showed mean TGM concentrations only insignificantly higher than the NC as a whole ($0.92\ \pm$

$0.04\ ng\ m^{-3}$ vs. $0.89 \pm 0.01\ ng\ m^{-3}$, $p = 0.067$, Mann-Whitney test). Admittingly, special care has to be taken

with air masses of this general direction, as they move frequently over the urban area of La Paz/El Alto (Chauvigné

et al., 2019) before arriving at CHC and could be punctually enriched in Hg, even though the city does overall not

seem to play an important role in average Hg concentrations (compare to TGM diel pattern, Fig. 4a). We evaluated

this possibility by excluding data with high eBC concentrations (> 87.5th eBC percentile of NC), apparently

Atmospheric
Chemistry
and Physics
Discussions

Open Access

EGU

694   strongly linked to urban pollution (Fig. 4c, Wiedensohler et al., 2018), without an apparent change in the above

695   results. Therefore, these elevated TGM concentrations in air masses passing over degassing volcanoes to the south

696   of CHC are unlikely caused by urban pollution on the way and might indeed be related to volcanic emissions.

697   On the other hand, TGM concentrations in air masses passing over the volcanoes Ubinas and Sabancaya to the

698   west of CHC did not appear to be significantly elevated, compared to air masses of similar origin (pollution map,

699   Fig. 6a), even though both volcanoes are currently strongly degassing and account combined for more than half

700   of the entire CVZ volatile fluxes, as estimated by Moussallam et al. (2017). They also lie in a frequent source

701   region for air masses arriving at CHC, especially in the dry season (Fig. 5).

702   Thus, our data provides an inconclusive picture of the role of the CVZ in the atmospheric mercury budget in the

703   region. While a volcanic mercury source south of CHC can be supported due to significantly elevated TGM

704   concentrations in the source region, we cannot say the same for volcanoes to the west of CHC, even though both

705   Ubinas and Sabancaya were strongly emitting other volcanic gases such as SO_2 during NC (Carn et al., 2017;

706   Moussallam et al., 2017). This inconsistency might be related to the complexity of volcanic mercury emissions,

707   whose quantity is highly variable between different volcanoes, their activity phase, and different points in time

708   (Bagnato et al., 2011; Ferrara et al., 2000). For instance, volcanic Hg/SO_2 emission ratios obtained in literature

709   span several orders of magnitude (Bagnato et al., 2015).

710

4.6 Artisanal and small scale gold mining (ASGM)

712   ASGM is known to be a major source of mercury pollution, especially important in Latin America (Esdaile and

713   Chalker, 2018; Obrist et al., 2018). According to recent inventories, South America contributes to 18% of global

714   Hg emissions to the atmosphere, with 80% of it deriving from the ASGM sector (UNEP GMA 2018). One

715   prominent ASGM hot spot on the continent is the "Madre de Dios" watershed, a few hundred kilometers north of

716   CHC station (Fig. 1), where high Hg concentrations have been found among others in sediments and human hair

717   (Langeland et al., 2017; Martinez et al., 2018).

718   As shown in Fig. 6b, we measured the highest TGM concentrations in northern Amazonian air masses (cluster

719   C1), which pass mostly over the "Madre de Dios" watershed. Notably, C1 air masses in the wet season showed

720   much higher mean Hg concentrations than the other important lowland cluster C2, which does not pass over this

721   region ($0.91 \pm 0.02 \, ng \, m^{-3}$ vs. $0.82 \pm 0.02 \, ng \, m^{-3}$, $p = 9.9 \cdot 10^{-12}$, Mann-Whitney test). Still, TGM

722   is uniformly high for most of the north/north-eastern lowland air masses, and the "Madre de Dios" region does

723   not actually appear distinctively in our pollution maps (Fig. 6a). This could be explained by ASGM scattered

724   rather evenly around a large part of the Bolivian lowlands, instead of being clustered around a few hot spots. This

725   is certainly not an unlikely scenario, but it has to be acknowledged that the techniques applied here might not

726   provide the necessary resolution to clearly discern isolated ASGM hotspots hundreds of kilometers away, given

727   dilution and diffusion processes and the uncertainties in HYSPLIT trajectories.

728

729

730

731 **5. Conclusions**

732 Our measurements of TGM at the mountain site CHC fill an important gap in observations for South America and

733 allow us to make justified assumptions about the dynamics of atmospheric mercury on the continent.

734 During NC, mean TGM concentrations at CHC were relatively low compared to other sites in the Southern

735 Hemisphere, but similar to those in South America. However, we detected a significant rise of atmospheric Hg

736 levels during EC, which might well be related to the 2015 – 2016 "El Niño", a hypothesis we will address in an

737 upcoming publication. In the regional overview, mercury concentrations were higher in air masses with northern

738 Amazonian or southern Altiplanic origin, the former possibly related to a strong ASGM presence in the source

739 region, while the latter might be of volcanic origin. In agreement with other South American sites, but in contrast

740 to different regions in the Southern Hemisphere, we observed a marked seasonal pattern. Concentrations were

741 lowest in the dry season (austral winter), rising in the BB season, and highest in the beginning of the wet season

742 (austral summer). To explain this, we explored several possible drivers for this seasonal cycle. Biomass burning

743 related Hg emissions appear to significantly raise atmospheric Hg levels during a limited time of the year, mainly

744 between August and October (BB season). Vegetation on the continent, most prominently the Amazon rainforest,

745 seems to act as an important mercury sink, at least during months of high gross primary production (around

746 February – April). Finally, arguments can be made for a significant influence of the Eastern Pacific Ocean on

747 regional Hg levels, possibly through a shift in ocean-atmosphere Hg exchanges in response to rising sea surface

748 temperature and deep convection in austral summer.

749 Notably, all three of these major regional drivers of atmospheric mercury might undergo significant changes in

750 the near future. On one hand, Pacific SST and convection dynamics could shift as a consequence of climate

751 change. On the other hand, both upcoming BB emissions and the magnitude of the South American vegetation

752 sink will depend heavily on the future of the Amazon rainforest, which itself is threatened by climate change and

753 changes in land-use, e.g., deforestation and agricultural practices. In perspective, the TGM/CO emission ratio and

754 TGM/CO_2 *uptake ratio* obtained here could be used to constrain both current and future South American biomass

755 burning Hg emissions and vegetation Hg uptake, with the help of remotely sensed CO and CO_2 data products and

756 model results.

757

758

759   **Appendix A: Seasonality of CO concentrations in South America and CHC**

(a)

(b)

760
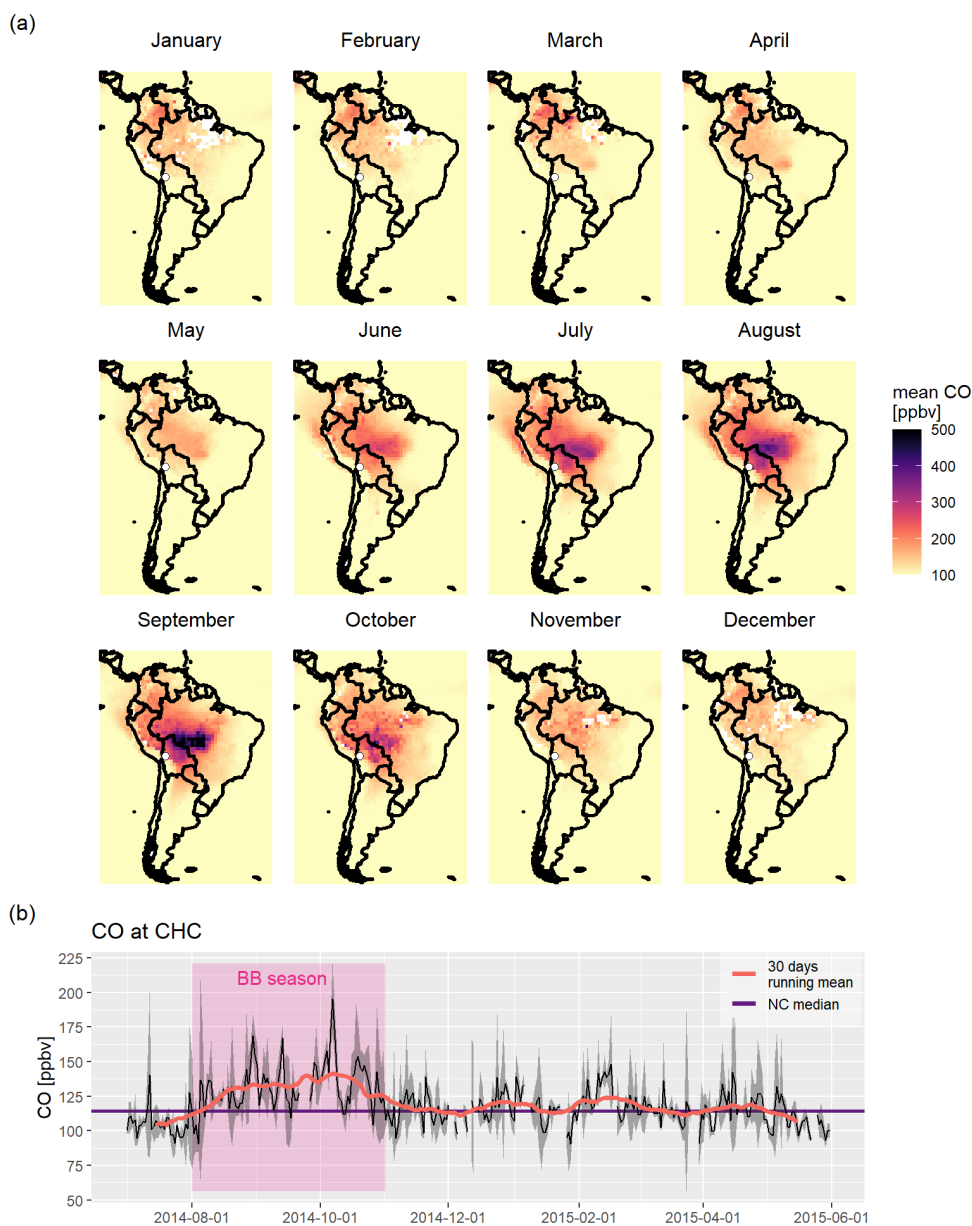
Fig. A1. (a) Seasonality of remotely sensed tropospheric CO concentrations in South America, from 01.2005 to

01.2015 and based on the MOP03J_V008 data product (Ziskin, 2019). The white dot shows the CHC station. (b)

Daily mean CO concentrations at CHC during "normal conditions" (NC: 2014-07-01 until 2015-06-01). Grey

shaded area shows the standard deviation, orange line the 30 days running mean, purple line the NC median.

The pink box illustrates the definition of the biomass burning (BB) season used in the present work.

Atmospheric
Chemistry
and Physics
Discussions

Appendix B: Pollution maps at different cutoff altitudes

766
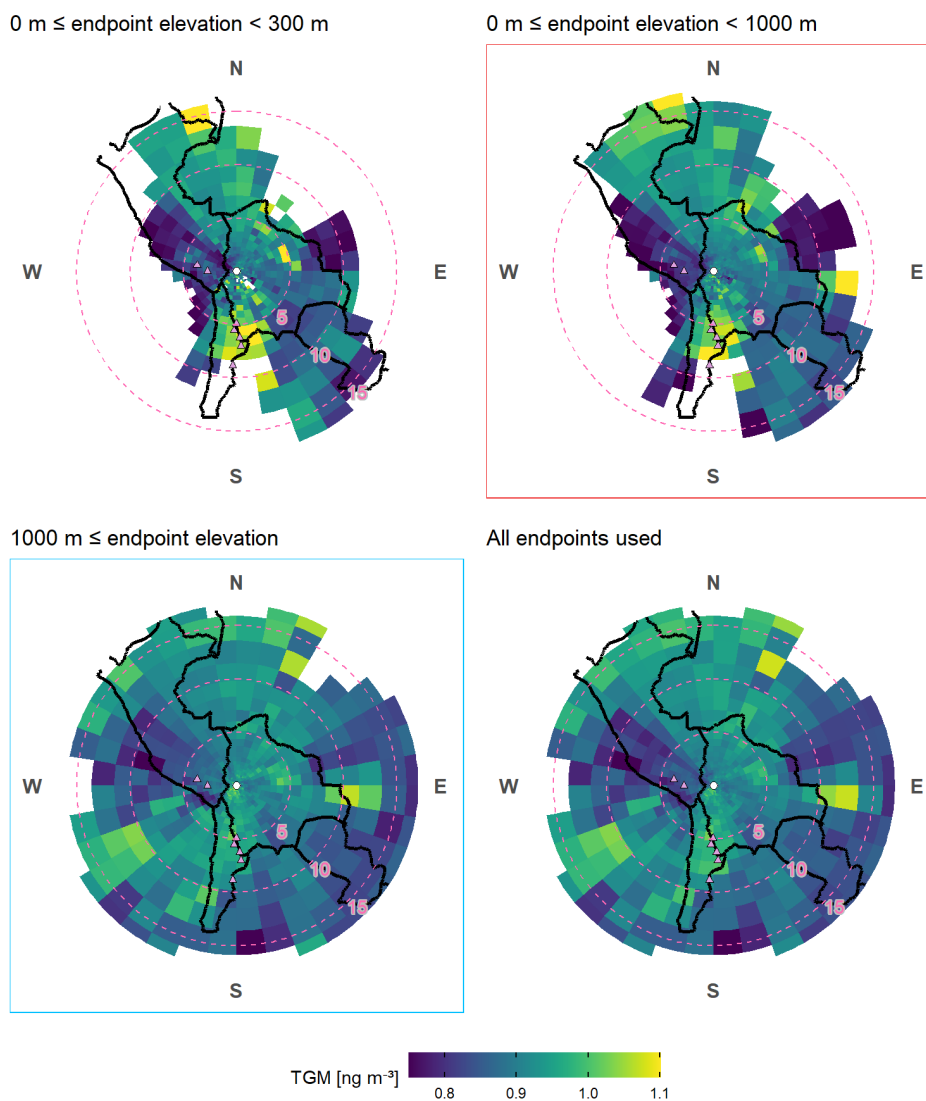
Fig. B1: Pollutions map based on all TGM data taken during NC, calculated by using different cutoff altitudes as specified by the plot title. The plot corresponding to the cutoff – altitude used in the main text (endpoint elevation < 1000 m a.g.l) is framed in red. The plot based on all endpoints which were excluded from the pollution map shown in the main text is framed in blue. Dashed range circles show distance to CHC in degrees. Color scale capped at the limits. Cells with less than 10 data points (n < 10) were excluded. Pink triangles show selected degassing volcanoes in the CVZ, from north to south: Sabancaya, Ubinas, Ollague, San Pedro, Putana, Lascar, Lastarria.

767
768
769
770
771
772
773
774
775
776

Atmospheric
Chemistry
and Physics
Discussions

777 **Appendix C: Median transport time for HYSPLIT back-trajectories arriving at CHC**
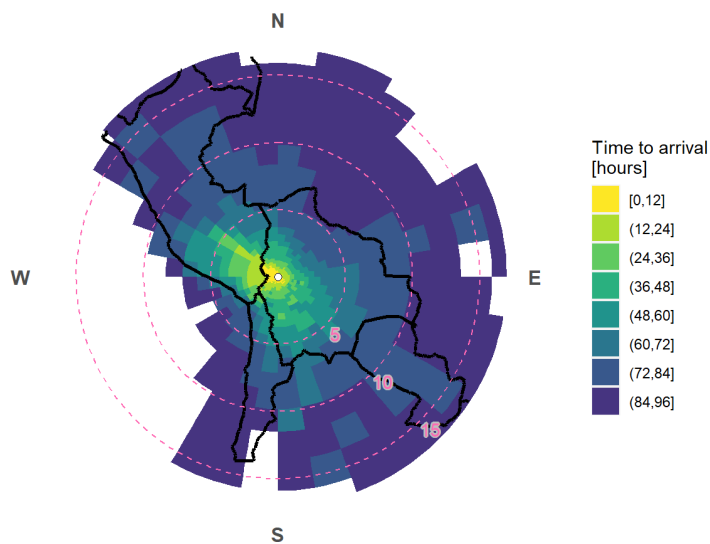
778

779 *Fig. C1: Average transport time between air mass source region and CHC, shown through the median time*
780 *passed between HYSPLIT trajectory pixel piercing and arrival at CHC. Distance to CHC (white dot) in degrees*
781 *is shown in dashed range circles. Based on all trajectories during NC (01.07.2014 - 01.06.2015) and endpoints*
782 *with an elevation below 1000 m a.g.l.*

783
784
785
786

Appendix D: Sensitivity analysis for the calculation of the TGM/CO emission ratio
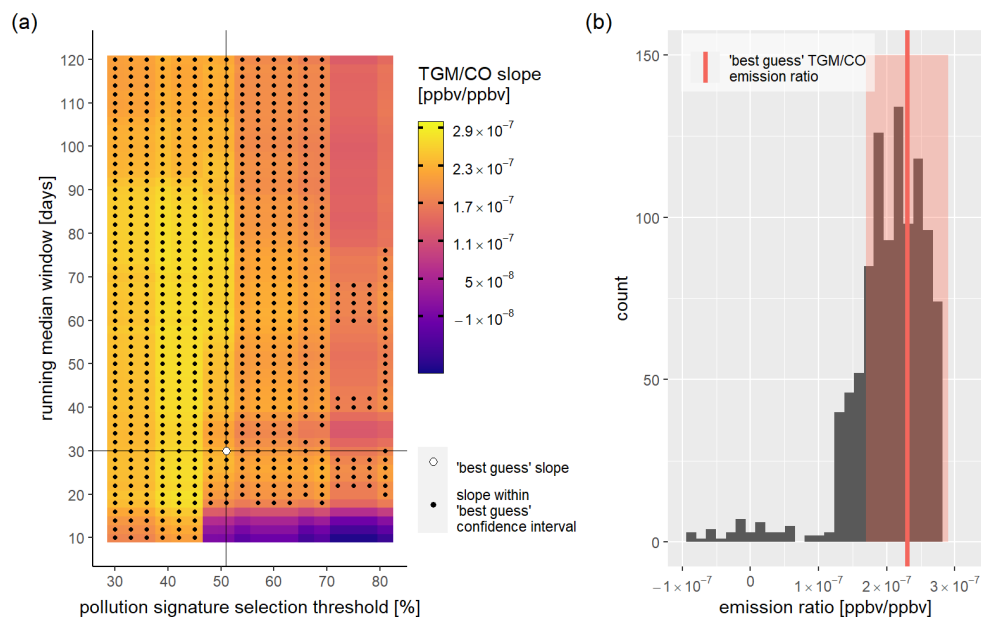
Fig. D1: Sensitivity analysis for the calculation of the TGM/CO emission ratio as a function of the chosen threshold for the selection of biomass burning pollution signatures (percentage of time the pollution signature fell into the BB season) and the choice on the size of the "running window" (in days) to calculate the median TGM background concentrations. (a) Heatmap showing the obtained TGM/CO emission ratios for a wide range of combinations of the pollution signature threshold (x-axis) and the running window (y-axis). "Best guess" TGM/CO emission ratio as presented in the main text marked as white dot, black dots show all combinations for which the calculated slope is within the "best guess" confidence interval. (b) Histogram for all TGM/CO slopes shown in (a) (the heatmap). "Best guess" emission ratio and its confidence interval in red.

Atmospheric
Chemistry
and Physics
Discussions

805

806 **Competing interests:**

807 The authors declare that they have no conflict of interest.

808

809 **Autor contribution:**

810 Alkuin Maximilian Koenig performed data analysis, prepared figures, and prepared the manuscript. Olivier
811 Magand collected TGM data, was part in scientific discussions, data interpretation, and the manuscript
812 preparation. Paolo Laj was part in scientific discussions and the manuscript preparation. Marcos Andrade
813 provided data, was part in scientific discussions, and the manuscript preparation. Isabel Moreno collected data,
814 was part in scientific discussions, and the manuscript preparation. Fernando Velarde collected data, was part in
815 scientific discussions, and the manuscript preparation. Grover Salvatierra collected data and performed data
816 analysis. René Gutierrez was part in data collection and scientific discussions. Luis Blacutt was part in scientific
817 discussions, and the manuscript preparation. Diego Aliaga performed data analysis, was part in scientific
818 discussions, and the manuscript preparation. Thomas Reichler was part in computation, scientific discussions,
819 and the manuscript preparation. Karine Sellegri provided data, was part in scientific discussions and the
820 manuscript preparation, Olivier Laurent collected data. Michel Ramonet provided data, was part in scientific
821 discussions and the manuscript preparation, Aurélien Dommergue designed the experiment, collected data, was
822 part in scientific discussions, and the manuscript preparation.

823

839 **References**

840 Ambrizzi, T., de Souza, E. B. and Pulwarty, R. S.: The Hadley and Walker Regional Circulations and

841 Associated ENSO Impacts on South American Seasonal Rainfall, in The Hadley Circulation: Present, Past and

842 Future, vol. 21, edited by H. F. Diaz and R. S. Bradley, pp. 203–235, Springer Netherlands, Dordrecht., 2004.

843 Andrade, M., Zaratti, F., Forno, R., Gutiérrez, R., Moreno, I., Velarde, F., Ávila, F., Roca, M., Sánchez, M. F.,

844 Laj, P., Jaffrezo, J. L., Ginot, P., Sellegri, K., Ramonet, M., Laurent, O., Weinhold, K., Wiedensohler, A.,

845 Krejci, R., Bonasoni, P., Cristofanelli, P., Whiteman, D., Vimeux, F., Dommergue, A., Magand, O. and M.

846 Andrade: Puesta en marcha de una nueva estación de monitoreo climático en los andes centrales de Bolivia: la

847 estación Gaw/Chacaltaya, Revista Boliviana de Física, 26, 6–15, 2015.

848 Angot, H., Barret, M., Magand, O., Ramonet, M. and Dommergue, A.: A 2-year record of atmospheric mercury

849 species at a background Southern Hemisphere station on Amsterdam Island, Atmos. Chem. Phys., 14(20),

850 11461–11473, doi:10.5194/acp-14-11461-2014, 2014.

851 Beal, S. A., Jackson, B. P., Kelly, M. A., Stroup, J. S. and Landis, J. D.: Effects of Historical and Modern

852 Mining on Mercury Deposition in Southeastern Peru, Environ. Sci. Technol., 47(22), 12715–12720,

853 doi:10.1021/es402317x, 2013.

854 Bloom, N. and Fitzgerald, W. F.: Determination of volatile mercury species at the picogram level by low-

855 temperature gas chromatography with cold-vapour atomic fluorescence detection, Analytica Chimica Acta, 208,

856 151–161, doi:10.1016/S0003-2670(00)80743-6, 1988.

857 Bond, T. C. and Bergstrom, R. W.: Light Absorption by Carbonaceous Particles: An Investigative Review,

858 Aerosol Science and Technology, 40(1), 27–67, doi:10.1080/02786820500421521, 2006.

859 Cape, J. N., Coyle, M. and Dumitrean, P.: The atmospheric lifetime of black carbon, Atmospheric Environment,

860 59, 256–263, doi:10.1016/j.atmosenv.2012.05.030, 2012.

861 Carbone, F., Landis, M. S., Gencarelli, C. N., Naccarato, A., Sprovieri, F., De Simone, F., Hedgecock, I. M. and

862 Pirrone, N.: Sea surface temperature variation linked to elemental mercury concentrations measured on Mauna

863 Loa: SST AND HG(0) CONCENTRATION ON MAUNA LOA, Geophys. Res. Lett., 43(14), 7751–7757,

864 doi:10.1002/2016GL069252, 2016.

865 Carn, S. A., Fioletov, V. E., McLinden, C. A., Li, C. and Krotkov, N. A.: A decade of global volcanic SO2

866 emissions measured from space, Sci Rep, 7(1), 44095, doi:10.1038/srep44095, 2017.

867 Chauvigné, A., Aliaga, D., Sellegri, K., Montoux, N., Krejci, R., Močnik, G., Moreno, I., Müller, T., Pandolfi,

868 M., Velarde, F., Weinhold, K., Ginot, P., Wiedensohler, A., Andrade, M. and Laj, P.: Biomass burning and

869 urban emission impacts in the Andes Cordillera region based on in situ measurements from the Chacaltaya

870 observatory, Bolivia (5240&#8201;m&#8201;a.s.l.), Atmos. Chem. Phys., 19(23), 14805–14824,

871 doi:10.5194/acp-19-14805-2019, 2019.

872 Choi, Y., Kanaya, Y., Park, S.-M., Matsuki, A., Sadanaga, Y., Kim, S.-W., Uno, I., Pan, X., Lee, M., Kim, H.

873 and Jung, D. H.: Regional variability in black carbon and carbon monoxide ratio from long-term observations

874   over East Asia: assessment of representativeness for black carbon (BC) and carbon monoxide (CO) emission

875   inventories, Atmos. Chem. Phys., 20(1), 83–98, doi:10.5194/acp-20-83-2020, 2020.

876   D'Amore, F., Bencardino, M., Cinnirella, S., Sprovieri, F. and Pirrone, N.: Data quality through a web-based

877   QA/QC system: implementation for atmospheric mercury data from the global mercury observation system,

878   Environ. Sci.: Processes Impacts, 17(8), 1482–1491, doi:10.1039/C5EM00205B, 2015.

879   Diéguez, M. C., Bencardino, M., García, P. E., D'Amore, F., Castagna, J., De Simone, F., Soto Cárdenas, C.,

880   Ribeiro Guevara, S., Pirrone, N. and Sprovieri, F.: A multi-year record of atmospheric mercury species at a

881   background mountain station in Andean Patagonia (Argentina): Temporal trends and meteorological influence,

882   Atmospheric Environment, 214, 116819, doi:10.1016/j.atmosenv.2019.116819, 2019.

883   Diringer, S. E., Feingold, B. J., Ortiz, E. J., Gallis, J. A., Araújo-Flores, J. M., Berky, A., Pan, W. K. Y. and

884   Hsu-Kim, H.: River transport of mercury from artisanal and small-scale gold mining and risks for dietary

885   mercury exposure in Madre de Dios, Peru, Environ. Sci.: Processes Impacts, 17(2), 478–487,

886   doi:10.1039/C4EM00567H, 2015.

887   Diringer, S. E., Berky, A. J., Marani, M., Ortiz, E. J., Karatum, O., Plata, D. L., Pan, W. K. and Hsu-Kim, H.:

888   Deforestation Due to Artisanal and Small-Scale Gold Mining Exacerbates Soil and Mercury Mobilization in

889   Madre de Dios, Peru, Environ. Sci. Technol., acs.est.9b06620, doi:10.1021/acs.est.9b06620, 2019.

890   Dumarey, R., Temmerman, E., Adams, R. and Hoste, J.: The accuracy of the vapour-injection calibration

891   method for the determination of mercury by amalgamation/cold-vapour atomic absorption spectrometry,

892   Analytica Chimica Acta, 170, 337–340, doi:10.1016/S0003-2670(00)81759-6, 1985.

893   Ebinghaus, R., Slemr, F., Brenninkmeijer, C. A. M., van Velthoven, P., Zahn, A., Hermann, M., O'Sullivan, D.

894   A. and Oram, D. E.: Emissions of gaseous mercury from biomass burning in South America in 2005 observed

895   during CARIBIC flights: HG EMISSION FROM BIOMASS BURNING, Geophys. Res. Lett., 34(8),

896   doi:10.1029/2006GL028866, 2007.

897   Erfanian, A., Wang, G. and Fomenko, L.: Unprecedented drought over tropical South America in 2016:

898   significantly under-predicted by tropical SST, Sci Rep, 7(1), 5811, doi:10.1038/s41598-017-05373-2, 2017.

899   Ericksen, J. A., Gustin, M. S., Schorran, D. E., Johnson, D. W., Lindberg, S. E. and Coleman, J. S.:

900   Accumulation of atmospheric mercury in forest foliage, Atmospheric Environment, 37(12), 1613–1622,

901   doi:10.1016/S1352-2310(03)00008-6, 2003.

902   Esdaile, L. J. and Chalker, J. M.: The Mercury Problem in Artisanal and Small-Scale Gold Mining, Chem. Eur.

903   J., 24(27), 6905–6916, doi:10.1002/chem.201704840, 2018.

904   Figueiredo, B. R., De Campos, A. B., Da Silva, R. and Hoffman, N. C.: Mercury sink in Amazon rainforest: soil

905   geochemical data from the Tapajos National Forest, Brazil, Environ Earth Sci, 77(8), 296, doi:10.1007/s12665-

906   018-7471-x, 2018.

907   Fitzgerald, W. F. and Gill, G. A.: Subnanogram determination of mercury by two-stage gold amalgamation and

908   gas phase detection applied to atmospheric analysis, Anal. Chem., 51(11), 1714–1720,

909   doi:10.1021/ac50047a030, 1979.

910   Fostier, A. H., Melendez-Perez, J. J. and Richter, L.: Litter mercury deposition in the Amazonian rainforest,
911   Environmental Pollution, 206, 605–610, doi:10.1016/j.envpol.2015.08.010, 2015.

912   Frankenberg, C., Fisher, J. B., Worden, J., Badgley, G., Saatchi, S. S., Lee, J.-E., Toon, G. C., Butz, A., Jung,
913   M., Kuze, A. and Yokota, T.: New global observations of the terrestrial carbon cycle from GOSAT: Patterns of
914   plant fluorescence with gross primary productivity: CHLOROPHYLL FLUORESCENCE FROM SPACE,
915   Geophys. Res. Lett., 38(17), n/a-n/a, doi:10.1029/2011GL048738, 2011.

916   Fraser, A., Dastoor, A. and Ryjkov, A.: How important is biomass burning in Canada to mercury
917   contamination?, Atmos. Chem. Phys., 18(10), 7263–7286, doi:10.5194/acp-18-7263-2018, 2018.

918   Graciela, A., Maria, K. and de Freitas, S. R.: Biomass Burning in South America: Transport Patterns and
919   Impacts, in Biomass - Detection, Production and Usage, edited by M. D. Matovic, InTech., 2011.

920   Grigal, D. F.: Mercury Sequestration in Forests and Peatlands: A Review, J. Environ. Qual., 32(2), 393–405,
921   doi:10.2134/jeq2003.3930, 2003.

922   Guédron, S., Point, D., Acha, D., Bouchet, S., Baya, P. A., Tessier, E., Monperrus, M., Molina, C. I., Groleau,
923   A., Chauvaud, L., Thebault, J., Amice, E., Alanoca, L., Duwig, C., Uzu, G., Lazzaro, X., Bertrand, A., Bertrand,
924   S., Barbraud, C., Delord, K., Gibon, F. M., Ibanez, C., Flores, M., Fernandez Saavedra, P., Ezpinoza, M. E.,
925   Heredia, C., Rocha, F., Zepita, C. and Amouroux, D.: Mercury contamination level and speciation inventory in
926   Lakes Titicaca & Uru-Uru (Bolivia): Current status and future trends, Environmental Pollution, 231, 262–270,
927   doi:10.1016/j.envpol.2017.08.009, 2017.

928   Horowitz, H. M., Jacob, D. J., Zhang, Y., Dibble, T. S., Slemr, F., Amos, H. M., Schmidt, J. A., Corbitt, E. S.,
929   Marais, E. A. and Sunderland, E. M.: A new mechanism for atmospheric mercury redox chemistry: implications
930   for the global mercury budget, Atmos. Chem. Phys., 17(10), 6353–6371, doi:10.5194/acp-17-6353-2017, 2017.

931   Howard, D., Nelson, P. F., Edwards, G. C., Morrison, A. L., Fisher, J. A., Ward, J., Harnwell, J., van der
932   Schoot, M., Atkinson, B., Chambers, S. D., Griffiths, A. D., Werczynski, S. and Williams, A. G.: Atmospheric
933   mercury in the southern hemisphere tropics: seasonal and diurnal variations and influence of inter-hemispheric
934   transport, preprint, Gases/Field Measurements/Troposphere/Chemistry (chemical composition and reactions).,
935   2017a.

936   Howard, D., Nelson, P. F., Edwards, G. C., Morrison, A. L., Fisher, J. A., Ward, J., Harnwell, J., van der
937   Schoot, M., Atkinson, B., Chambers, S. D., Griffiths, A. D., Werczynski, S. and Williams, A. G.: Atmospheric
938   mercury in the Southern Hemisphere tropics: seasonal and diurnal variations and influence of inter-hemispheric
939   transport, Atmos. Chem. Phys., 17(18), 11623–11636, doi:10.5194/acp-17-11623-2017, 2017b.

940   Jiskra, M., Wiederhold, J. G., Skyllberg, U., Kronberg, R.-M., Hajdas, I. and Kretzschmar, R.: Mercury
941   Deposition and Re-emission Pathways in Boreal Forest Soils Investigated with Hg Isotope Signatures, Environ.
942   Sci. Technol., 49(12), 7188–7196, doi:10.1021/acs.est.5b00742, 2015.

943   Jiskra, M., Sonke, J. E., Obrist, D., Bieser, J., Ebinghaus, R., Myhre, C. L., Pfaffhuber, K. A., Wängberg, I.,
944   Kyllönen, K., Worthy, D., Martin, L. G., Labuschagne, C., Mkololo, T., Ramonet, M., Magand, O. and

945 Dommergue, A.: A vegetation control on seasonal variations in global atmospheric mercury concentrations,

946 Nature Geosci, 11(4), 244–250, doi:10.1038/s41561-018-0078-8, 2018.

947 Khalil, M. A. K. and Rasmussen, R. A.: The global cycle of carbon monoxide: Trends and mass balance,

948 Chemosphere, 20(1–2), 227–242, doi:10.1016/0045-6535(90)90098-E, 1990.

949 Kooreman, M. L., Boersma, K. F., van Schaik, E., van Versendaal, R., Cacciari, A. and Tuinder, O. N. E.:

950 SIFTER sun-induced vegetation fluorescence data from GOME-2A (Version 2.0), , doi:10.21944/GOME2A-

951 SIFTER-V2-SUN-INDUCED-FLUORESCENCE, 2020.

952 Koren, G., van Schaik, E., Araújo, A. C., Boersma, K. F., Gärtner, A., Killaars, L., Kooreman, M. L., Kruijt, B.,

953 van der Laan-Luijkx, I. T., von Randow, C., Smith, N. E. and Peters, W.: Widespread reduction in sun-induced

954 fluorescence from the Amazon during the 2015/2016 El Niño, Phil. Trans. R. Soc. B, 373(1760), 20170408,

955 doi:10.1098/rstb.2017.0408, 2018.

956 Langeland, A., Hardin, R. and Neitzel, R.: Mercury Levels in Human Hair and Farmed Fish near Artisanal and

957 Small-Scale Gold Mining Communities in the Madre de Dios River Basin, Peru, IJERPH, 14(3), 302,

958 doi:10.3390/ijerph14030302, 2017.

959 Leduc, G., Vidal, L., Tachikawa, K., Rostek, F., Sonzogni, C., Beaufort, L. and Bard, E.: Moisture transport

960 across Central America as a positive feedback on abrupt climatic changes, Nature, 445(7130), 908–911,

961 doi:10.1038/nature05578, 2007.

962 Luus, K. A., Commane, R., Parazoo, N. C., Benmergui, J., Euskirchen, E. S., Frankenberg, C., Joiner, J.,

963 Lindaas, J., Miller, C. E., Oechel, W. C., Zona, D., Wofsy, S. and Lin, J. C.: Tundra photosynthesis captured by

964 satellite-observed solar-induced chlorophyll fluorescence, Geophys. Res. Lett., 44(3), 1564–1573,

965 doi:10.1002/2016GL070842, 2017.

966 Martin, L. G., Labuschagne, C., Brunke, E.-G., Weigelt, A., Ebinghaus, R. and Slemr, F.: Trend of atmospheric

967 mercury concentrations at Cape Point for 1995–2004 and since 2007, Atmos. Chem. Phys., 17(3), 2393–2399,

968 doi:10.5194/acp-17-2393-2017, 2017.

969 Michelazzo, P. A. M., Fostier, A. H., Magarelli, G., Santos, J. C. and de Carvalho, J. A.: Mercury emissions

970 from forest burning in southern Amazon: MERCURY EMISSIONS FROM FOREST BURNING, Geophys.

971 Res. Lett., 37(9), n/a-n/a, doi:10.1029/2009GL042220, 2010.

972 Morgan, W. T., Darbyshire, E., Spracklen, D. V., Artaxo, P. and Coe, H.: Non-deforestation drivers of fires are

973 increasingly important sources of aerosol and carbon dioxide emissions across Amazonia, Sci Rep, 9(1), 16975,

974 doi:10.1038/s41598-019-53112-6, 2019.

975 Moussallam, Y., Tamburello, G., Peters, N., Apaza, F., Schipper, C. I., Curtis, A., Aiuppa, A., Masias, P.,

976 Boichu, M., Bauduin, S., Barnie, T., Bani, P., Giudice, G. and Moussallam, M.: Volcanic gas emissions and

977 degassing dynamics at Ubinas and Sabancaya volcanoes; implications for the volatile budget of the central

978 volcanic zone, Journal of Volcanology and Geothermal Research, 343, 181–191,

979 doi:10.1016/j.jvolgeores.2017.06.027, 2017.

980   Müller, D., Wip, D., Warneke, T., Holmes, C. D., Dastoor, A. and Notholt, J.: Sources of atmospheric mercury
981   in the tropics: continuous observations at a coastal site in Suriname, Atmos. Chem. Phys., 12(16), 7391–7397,
982   doi:10.5194/acp-12-7391-2012, 2012.

983   Müller, T., Henzing, J. S., de Leeuw, G., Wiedensohler, A., Alastuey, A., Angelov, H., Bizjak, M., Collaud
984   Coen, M., Engström, J. E., Gruening, C., Hillamo, R., Hoffer, A., Imre, K., Ivanow, P., Jennings, G., Sun, J. Y.,
985   Kalivitis, N., Karlsson, H., Komppula, M., Laj, P., Li, S.-M., Lunder, C., Marinoni, A., Martins dos Santos, S.,
986   Moerman, M., Nowak, A., Ogren, J. A., Petzold, A., Pichon, J. M., Rodriquez, S., Sharma, S., Sheridan, P. J.,
987   Teinilä, K., Tuch, T., Viana, M., Virkkula, A., Weingartner, E., Wilhelm, R. and Wang, Y. Q.: Characterization
988   and intercomparison of aerosol absorption photometers: result of two intercomparison workshops, Atmos. Meas.
989   Tech., 4(2), 245–268, doi:10.5194/amt-4-245-2011, 2011.

990   Obrist, D.: Atmospheric mercury pollution due to losses of terrestrial carbon pools?, Biogeochemistry, 85(2),
991   119–123, doi:10.1007/s10533-007-9108-0, 2007.

992   Obrist, D., Kirk, J. L., Zhang, L., Sunderland, E. M., Jiskra, M. and Selin, N. E.: A review of global
993   environmental mercury processes in response to human and natural perturbations: Changes of emissions,
994   climate, and land use, Ambio, 47(2), 116–140, doi:10.1007/s13280-017-1004-9, 2018.

995   Park, R. J.: Export efficiency of black carbon aerosol in continental outflow: Global implications, J. Geophys.
996   Res., 110(D11), D11205, doi:10.1029/2004JD005432, 2005.

997   Perez Catán, S., Bubach, D., Messuti, M. I., Arribére, M. A. and Ribeiro Guevara, S.: Mercury in a geothermal
998   and volcanic area in Patagonia, southern South America, Atmospheric Pollution Research, 11(3), 566–573,
999   doi:10.1016/j.apr.2019.12.005, 2020.

1000   Petzold, A. and Schönlinner, M.: Multi-angle absorption photometry—a new method for the measurement of
1001   aerosol light absorption and atmospheric black carbon, Journal of Aerosol Science, 35(4), 421–441,
1002   doi:10.1016/j.jaerosci.2003.09.005, 2004.

1003   Phillips, O. L., Lewis, S. L., Baker, T. R., Chao, K.-J. and Higuchi, N.: The changing Amazon forest, Phil.
1004   Trans. R. Soc. B, 363(1498), 1819–1827, doi:10.1098/rstb.2007.0033, 2008.

1005   Qiu, R., Han, G., Ma, X., Xu, H., Shi, T. and Zhang, M.: A Comparison of OCO-2 SIF, MODIS GPP, and
1006   GOSIF Data from Gross Primary Production (GPP) Estimation and Seasonal Cycles in North America, Remote
1007   Sensing, 12(2), 258, doi:10.3390/rs12020258, 2020.

1008   Rose, C., Sellegri, K., Velarde, F., Moreno, I., Ramonet, M., Weinhold, K., Krejci, R., Ginot, P., Andrade, M.,
1009   Wiedensohler, A. and Laj, P.: Frequent nucleation events at the high altitude station of Chacaltaya (5240 m
1010   a.s.l.), Bolivia, Atmospheric Environment, 102, 18–29, doi:10.1016/j.atmosenv.2014.11.015, 2015.

1011   Rose, C., Sellegri, K., Moreno, I., Velarde, F., Ramonet, M., Weinhold, K., Krejci, R., Andrade, M.,
1012   Wiedensohler, A., Ginot, P. and Laj, P.: CCN production by new particle formation in the free troposphere,
1013   Atmos. Chem. Phys., 17(2), 1529–1541, doi:10.5194/acp-17-1529-2017, 2017.

1014   Sanders, A., Verstraeten, W., Kooreman, M., van Leth, T., Beringer, J. and Joiner, J.: Spaceborne Sun-Induced

1015   Vegetation Fluorescence Time Series from 2007 to 2015 Evaluated with Australian Flux Tower Measurements,

1016   Remote Sensing, 8(11), 895, doi:10.3390/rs8110895, 2016.

1017   Shi, Y., Zhao, A., Matsunaga, T., Yamaguchi, Y., Zang, S., Li, Z., Yu, T. and Gu, X.: High-resolution inventory

1018   of mercury emissions from biomass burning in tropical continents during 2001–2017, Science of The Total

1019   Environment, 653, 638–648, doi:10.1016/j.scitotenv.2018.10.420, 2019.

1020   Slemr, F., Ebinghaus, R., Brenninkmeijer, C. A. M., Hermann, M., Kock, H. H., Martinsson, B. G., Schuck, T.,

1021   Sprung, D., van Velthoven, P., Zahn, A. and Ziereis, H.: Gaseous mercury distribution in the upper troposphere

1022   and lower stratosphere observed onboard the CARIBIC passenger aircraft, Atmos. Chem. Phys., 9(6), 1957–

1023   1969, doi:10.5194/acp-9-1957-2009, 2009.

1024   Slemr, F., Angot, H., Dommergue, A., Magand, O., Barret, M., Weigelt, A., Ebinghaus, R., Brunke, E.-G.,

1025   Pfaffhuber, K. A., Edwards, G., Howard, D., Powell, J., Keywood, M. and Wang, F.: Comparison of mercury

1026   concentrations measured at several sites in the Southern Hemisphere, Atmos. Chem. Phys., 15(6), 3125–3133,

1027   doi:10.5194/acp-15-3125-2015, 2015.

1028   Slemr, F., Weigelt, A., Ebinghaus, R., Kock, H. H., Bödewadt, J., Brenninkmeijer, C. A. M., Rauthe-Schöch,

1029   A., Weber, S., Hermann, M., Becker, J., Zahn, A. and Martinsson, B.: Atmospheric mercury measurements

1030   onboard the CARIBIC passenger aircraft, Atmos. Meas. Tech., 9(5), 2291–2302, doi:10.5194/amt-9-2291-2016,

1031   2016.

1032   Slemr, F., Martin, L., Labuschagne, C., Mkololo, T., Angot, H., Magand, O., Dommergue, A., Garat, P.,

1033   Ramonet, M. and Bieser, J.: Atmospheric mercury in the Southern Hemisphere – Part 1: Trend and inter-annual

1034   variations in atmospheric mercury at Cape Point, South Africa, in 2007–2017, and on Amsterdam Island in

1035   2012–2017, Atmos. Chem. Phys., 20(13), 7683–7692, doi:10.5194/acp-20-7683-2020, 2020.

1036   Soerensen, A. L., Mason, R. P., Balcom, P. H., Jacob, D. J., Zhang, Y., Kuss, J. and Sunderland, E. M.:

1037   Elemental Mercury Concentrations and Fluxes in the Tropical Atmosphere and Ocean, Environ. Sci. Technol.,

1038   48(19), 11312–11319, doi:10.1021/es503109p, 2014.

1039   Sprovieri, F., Pirrone, N., Bencardino, M., D'Amore, F., Carbone, F., Cinnirella, S., Mannarino, V.,

1040   Landis, M., Ebinghaus, R., Weigelt, A., Brunke, E.-G., Labuschagne, C., Martin, L., Munthe, J., Wängberg, I.,

1041   Artaxo, P., Morais, F., Barbosa, H. de M. J., Brito, J., Cairns, W., Barbante, C., Diéguez, M. del C., Garcia, P.

1042   E., Dommergue, A., Angot, H., Magand, O., Skov, H., Horvat, M., Kotnik, J., Read, K. A., Neves, L. M.,

1043   Gawlik, B. M., Sena, F., Mashyanov, N., Obolkin, V., Wip, D., Feng, X. B., Zhang, H., Fu, X., Ramachandran,

1044   R., Cossa, D., Knoery, J., Marusczak, N., Nerentorp, M. and Norstrom, C.: Atmospheric mercury concentrations

1045   observed at ground-based monitoring sites globally distributed in the framework of the GMOS network, Atmos.

1046   Chem. Phys., 16(18), 11915–11935, doi:10.5194/acp-16-11915-2016, 2016.

1047   Stein, A. F., Draxler, R. R., Rolph, G. D., Stunder, B. J. B., Cohen, M. D. and Ngan, F.: NOAA's HYSPLIT

1048   Atmospheric Transport and Dispersion Modeling System, Bull. Amer. Meteor. Soc., 96(12), 2059–2077,

1049   doi:10.1175/BAMS-D-14-00110.1, 2015.

Atmospheric
Chemistry
and Physics
Discussions

1050   Subramanian, R., Kok, G. L., Baumgardner, D., Clarke, A., Shinozuka, Y., Campos, T. L., Heizer, C. G.,

1051   Stephens, B. B., de Foy, B., Voss, P. B. and Zaveri, R. A.: Black carbon over Mexico: the effect of atmospheric

1052   transport on mixing state, mass absorption cross-section, and BC/CO ratios, Atmos. Chem. Phys., 10(1), 219–

1053   237, doi:10.5194/acp-10-219-2010, 2010.

1054   Swartzendruber, P. C., Jaffe, D. A. and Finley, B.: Improved fluorescence peak integration in the Tekran 2537

1055   for applications with sub-optimal sample loadings, Atmospheric Environment, 43(22–23), 3648–3651,

1056   doi:10.1016/j.atmosenv.2009.02.063, 2009.

1057   Tamburello, G., Hansteen, T. H., Bredemeyer, S., Aiuppa, A. and Tassi, F.: Gas emissions from five volcanoes

1058   in northern Chile and implications for the volatiles budget of the Central Volcanic Zone: Volatiles budget of the

1059   CVZ, Chile, Geophys. Res. Lett., 41(14), 4961–4969, doi:10.1002/2014GL060653, 2014.

1060   Tassi, F., Aguilera, F., Vaselli, O., Darrah, T. and Medina, E.: Gas discharges from four remote volcanoes in

1061   northern Chile (Putana, Olca, Irruputuncu and Alitar): a geochemical survey, Annals of Geophysics, (2),

1062   doi:10.4401/ag-5173, 2011.

1063   Venables, W. N. and Ripley, B. D.: Modern Applied Statistics with S, Springer New York, New York, NY.,

1064   2002.

1065   Weisspenzias, P., Jaffe, D., Swartzendruber, P., Hafner, W., Chand, D. and Prestbo, E.: Quantifying Asian and

1066   biomass burning sources of mercury using the Hg/CO ratio in pollution plumes observed at the Mount Bachelor

1067   observatory, Atmospheric Environment, 41(21), 4366–4379, doi:10.1016/j.atmosenv.2007.01.058, 2007.

1068   Wiedensohler, A., Andrade, M., Weinhold, K., Müller, T., Birmili, W., Velarde, F., Moreno, I., Forno, R.,

1069   Sanchez, M. F., Laj, P., Ginot, P., Whiteman, D. N., Krejci, R., Sellegri, K. and Reichler, T.: Black carbon

1070   emission and transport mechanisms to the free troposphere at the La Paz/El Alto (Bolivia) metropolitan area

1071   based on the Day of Census (2012), Atmospheric Environment, 194, 158–169,

1072   doi:10.1016/j.atmosenv.2018.09.032, 2018.

1073   Yuan, W., Sommar, J., Lin, C.-J., Wang, X., Li, K., Liu, Y., Zhang, H., Lu, Z., Wu, C. and Feng, X.: Stable

1074   Isotope Evidence Shows Re-emission of Elemental Mercury Vapor Occurring after Reductive Loss from

1075   Foliage, Environ. Sci. Technol., 53(2), 651–660, doi:10.1021/acs.est.8b04865, 2019.

1076   Zhang, Y., Guanter, L., Berry, J. A., Joiner, J., van der Tol, C., Huete, A., Gitelson, A., Voigt, M. and Köhler,

1077   P.: Estimation of vegetation photosynthetic capacity from space-based measurements of chlorophyll

1078   fluorescence for terrestrial biosphere models, Glob Change Biol, 20(12), 3727–3742, doi:10.1111/gcb.12664,

1079   2014.

1080   Zhu, C., Kanaya, Y., Yoshikawa-Inoue, H., Irino, T., Seki, O. and Tohjima, Y.: Sources of atmospheric black

1081   carbon and related carbonaceous components at Rishiri Island, Japan: The roles of Siberian wildfires and of crop

1082   residue burning in China, Environmental Pollution, 247, 55–63, doi:10.1016/j.envpol.2019.01.003, 2019.

1083   Ziskin, D.: Measurements Of Pollution In The Troposphere (MOPITT) Level 3 Gridded Daily CO Retrievals

1084   (Thermal Infrared Radiances) (MOP03J) V008, , doi:10.5067/TERRA/MOPITT/MOP03J_L3.008, 2019.

1085